Modelling of a Fast EQE Measurement System

Manoj Payani

TU Delft

Modelling of a Fast EQE Measurement System

by

Manoj Payani

in partial fulfillment of the requirements for the Master of Science

Sustainable Energy Technology

at the Delft University of Technology,
to be defended publicly on Thursday August 30, 2018 at 15:30 hours.

Student number:	4614429		
Project duration:	Oct 2017 - Aug 2018		
Thesis committee:	Olindo Isabella	TU Delft, ESE - PVMD	Supervisor
	Rudi Santbergen	TU Delft, ESE - PVMD	Daily supervisor
	Stefaan Heirman	TU Delft, ESE - PVMD	Daily supervisor
	Miro Zeman	TU Delft, ESE - PVMD	Head of the ESE Department
	Jianning Dong	TU Delft, ESE - DCE&S	External committee member

This thesis is confidential and cannot be made public until August 30, 2018.

Abstract

External Quantum Efficiency (EQE) is an important performance measure parameter of a solar cell. EQE characterization gives deeper insights into the opto-electrical properties, current generation and recombination mechanisms in solar cells. Conventional EQE characterization of solar cells are done using a monochromator and lock-in amplifier. These measurements take a few minutes to completely resolve the spectral response of a solar cell in the visible and near infrared (VIS/NIR) region of the spectrum. Having faster EQE measurement setups will aid in faster solar cell characterization both in research and industrial production environments.

In this work a promising fast EQE measurement prototype called Fast Optical Measurement System (FOMS) developed by Delft Spectral Technologies (DST) is investigated. The FOMS prototype currently can operate only with a modulation scheme (a sequence of images) based on Michelson interferometer. The FOMS prototype hence cannot test other more suitable modulation schemes. To overcome this limitation a model to mimic the working of the FOMS prototype was developed by characterizing the existing setup which involved spectral distribution and intensity variations measurements. Various sub-functions were developed based on the characterization results and they were used to develop the model that could predict the spectrum on each pixel of the image loaded on the system. The developed model takes images corresponding to different modulation schemes as input and predicts the current output for each image. The model was finally validated by generating a new modulation scheme based on monochromatic EQE system. The percentage error in the current generated by the model and the prototype was around 3% which is within permissible limits.

In the future the developed model can serve as a tool to quickly test new modulation schemes that can make the FOMS prototype faster and more accurate. Further research with respect to developing images based on more suitable modulation schemes can help avoid the mathematical complexities in the Michelson interferometer based modulation scheme. Developing appropriate post-processing steps to complement the modulation schemes will help in obtaining the EQE characteristics of the device under test from the current predicted by the model.

Contents

List of Figures

Glossary

List of Acronyms

EQE	External Quantum Efficiency
UV	Ultraviolet
VIS	Visible
IR	Infrared
FTPS	Fourier Transform Photocurrent Spectroscopy
FOMS	Fast Optical Measurement System
DMD	Digital Micromirror Device
ADC	Analog to Digital converter
FTIR	Fourier transform infrared
FTS	Fourier transform Spectroscopy
I-V	Current-Voltage
QE	Quantum Efficiency
SR	Spectral Responsivity
FWHM	Full Width Half Maximum
DUT	Device under test

Acknowledgements

I must acknowledge the contributions of many people who have helped during my thesis: first and foremost, my Daily Supervisors - Rudi Santbergen and Stefaan Heirman. My sincere thanks to Rudi Santbergen for helping me deftly navigate past occasional obstacles that cropped up during my thesis and his excellent supervision. His reassuring and optimistic words during the back-end of my thesis, his calm and tranquil personality will be something I will try to emulate in life. To Stefaan, for being supportive during the initial experimental stages of my thesis, his patience to answer my many questions and help me understand the Fast Optical Measurement System is ineffable. A very special thank you also to the Delft Spectral Technologies team - Dr. Jimmy Melskens, Marc Schouten and Remko Koornneef for their support and taking time during their weekends to assist me during the thesis period. A debt of gratitude also to my Supervisor Dr. Olindo Isabella for his helpful feedback and giving me the space and time to grow at my pace. Thanks also to Prof. Dr. Miro Zeman and Dr. Jianning Dong for accepting to be part of my thesis committee.

During my stay here at the Technical University of Delft as a graduate student, I was fortunate to have been in the company of wonderful people. To Thomas Loef, Chris van Nierop, Paolo Maggioni, Julen Garro, Andres Calcabrini, Esteban David, Simona Villa - you guys have been a great support. A big thank you to you guys. I am very grateful to my dear friends Arun Meyappan, Santhosh Malagi and Santhosh Shetty for their wise counsel and being role models of grace and kindness. You guys have been my family away from home during my time here. Words cannot express my appreciation to Sunil Suresh, for his assistance during different stages of my study and also for both keeping me grounded and also pushing me to greater heights. Many thanks also to my engineering friends - Maadhav, Nayana, Abhiram and Anirudh Deshpande for being there both professionally and personally and sharing many life advises.

And finally I would like to express my gratitude and heartfelt thanks to my family. Amma, Appa and Pavan - If I am something today, it is only because of you people. My journey at Delft would not have been possible without your support and you will remain my greatest strength.

Manoj Payani
Delft, August 2018

[1]

[1] P.S - Coverpage photo from pixabay imaging website.

1

Introduction

Most of the modern world uses fossil fuels as the primary source of energy with coal, oil and natural gas accounting for over 80% of the energy consumption (figure 1.1) [1]. These energy sources are abundant, easy to transport and have very high energy density values compared to Renewable energy sources like Solar and Wind energy. However, they have adverse effects on human health and environment – including air and water pollution [2]. Climate change and rapidly declining fossil fuel resources are the major global challenges the world is currently facing [3]. The need of the hour is thus clean renewable energy to power our lives – with Solar and Wind energy leading the way. The emerging super powers of the world, India and China lie in the tropical belt and Solar energy seems the logical choice to satisfy their constantly increasing energy needs [4]. China has recently become the manufacturing hub for solar manufacturing industry and is adding solar power at a record pace [5]. India on the other hand is the second fastest growing renewable energy market after China in the world (figure 1.2) [6, 7]

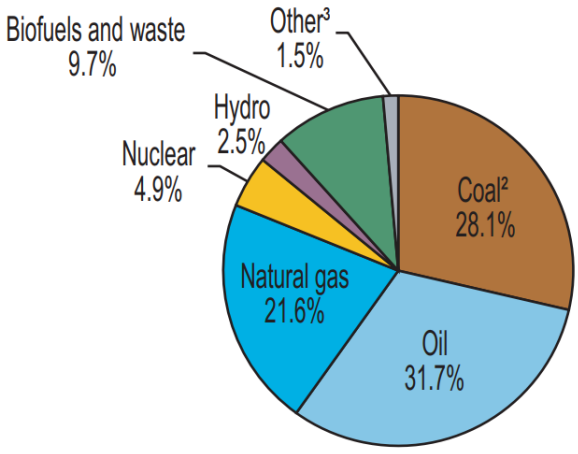

Figure 1.1: World Total Primary energy supply (TPES) by fuel shares - Fossil fuel contributes to about 81.4% of the world's total primary energy supply [1].

The role of solar photovoltaics (PV) in the world's future energy mix has been acknowledged and supported by governments around the world, which has led the PV industry to become the fastest growing market with an annual growth of 40% between 2010 and 2016 [8]. In order to meet this growing demand in solar PV, production rates have also significantly increased to around 1800 wafers per hour for a single production line [9].

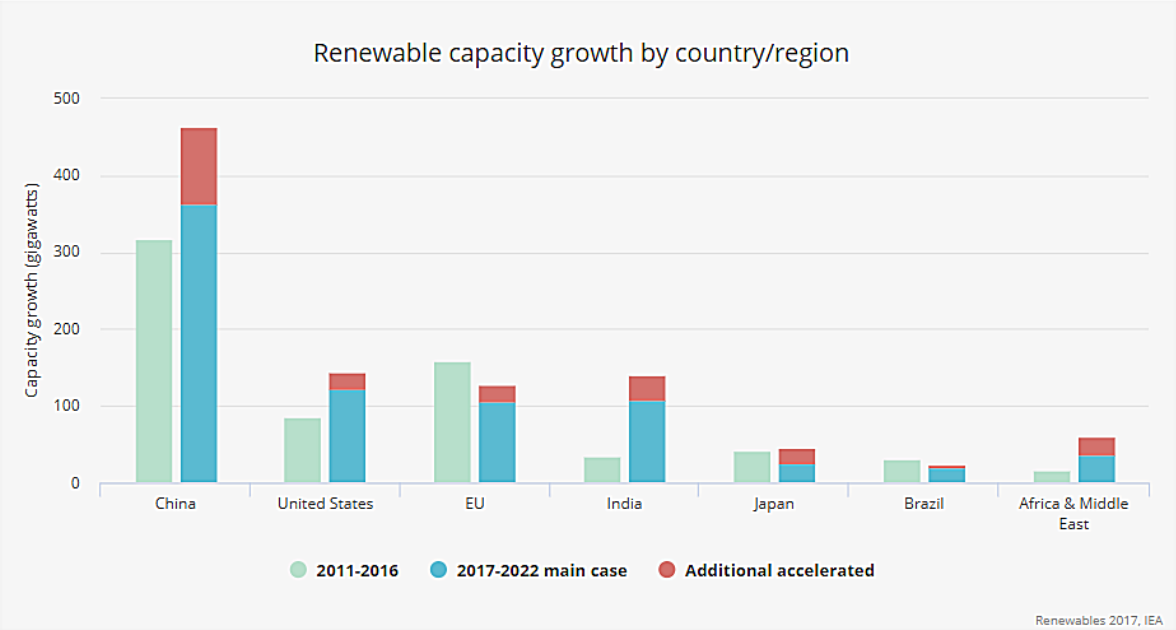

Figure 1.2: Renewable Energy capacity growth by country/region - China and India are the fastest growing markets for Renewable Energy [7].

To ensure consistent, uniform and efficient solar panels production in order to meet the ever increasing demand, solar cells used in panels have to be tested for their current-voltage (I-V) and external quantum efficiency (EQE) characteristics which form the basis of PV research [9]. The I-V measurements and the EQE characteristics are used both in research and development (R&D) of new cell structures and for reproducibility verification in industrial scale production of solar cells.

The I-V curve of a solar cell describes the energy conversion capability at different illuminations and external temperature conditions. It provides information on the solar cell parameters like short circuit current (I_{SC}), open circuit voltage of the cell (V_{OC}), the fill factor (FF), power conversion efficiency of the cell (η) and maximum power (P_{MPP}) that can be extracted from a solar cell. To allow comparisons between cells, I-V curve measurements are reported at Standard Testing Conditions (STC). The standard reference spectrum for the STC is AM 1.5 solar spectrum with an irradiance of 1000 W/m^2 and operating temperature of 25°C [10].

The Quantum Efficiency (QE) measurement in simple terms is an indicator of how well a solar cell converts sunlight into electricity as a function of the wavelength of incident light. The QE measurement is a standard method to gain deeper insights into the opto-electrical properties and for understanding current generation, recombination and diffusion mechanisms in photovoltaic devices. In academia the QE measurements are mainly used to evaluate quality of emitter layer, the charge carrier diffusion lengths, the passivation scheme used for different solar cells, for studying the defect densities within the active layer of a device etc [9, 11].

If all the photons of a certain wavelength are absorbed by the solar cell and all the resulting charge carriers are collected, then the QE at that particular wavelength is 100%. Also, the QE for photons with energy below the bandgap of the solar cell material is zero, due to the inability of the semiconductor to absorb photons with energy lesser than the bandgap i.e., the photons do not have sufficient energy for the creation of electron-hole pair in the semiconductor device. These photons pass through the solar cell as if it were transparent. The ideal QE curve of a solar cell will be square shaped as shown in the figure 1.3. However, the QE curve for most solar cell is not ideal and is determined by the optical and electrical losses in the solar cell like shading losses, parasitic absorption of incident light, recombination losses, transmission losses etc [10]. The final QE of the

cell depends on three major phenomena: the absorption of light creating the free charge carriers (electrons), the loss of the photo-generated excess charge carriers due to recombination and the electrical transport of these carriers that contribute to current from the cell.

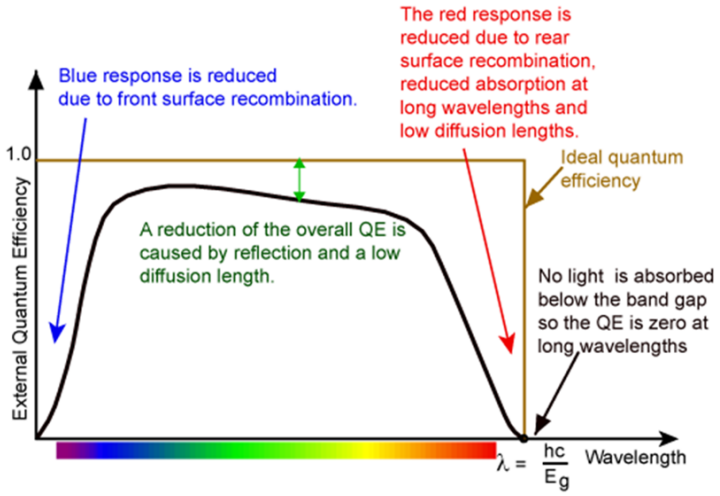

Figure 1.3: Comparison between the EQE curves of an ideal solar cell and a silicon solar cell [12].

Often two types of quantum efficiencies are considered for a solar cell – External Quantum Efficiency (EQE) and Internal Quantum Efficiency (IQE).

- **External Quantum Efficiency (EQE)** – It includes the effect of optical losses such as transmission through the cell and reflection of light at the top of the cell. It is defined as the ratio of number of charge carriers collected to the number of incident photons on the device active area at the given wavelength [10].
- **Internal Quantum Efficiency (IQE)** – It refers to the efficiency under the exclusion of transmitted or reflected light by the solar cell. It is defined as the ratio of number of charge carriers collected to the number of absorbed photons in the active layer at the given wavelength [10].

By measuring the reflection and transmission of a solar cell, the EQE curve can be adjusted to obtain the IQE curve. Since the absorbed light is typically lesser than the incident light - due to losses associated with reflection and transmission, the IQE of a solar cell is generally higher than the EQE. The difference between the IQE and EQE is important to distinguish the loss mechanisms between optical absorption properties of the entire device and photo conversion properties of the absorbing material [10].

Additionally the spectral response (SR) measurements are often used interchangeably with the Quantum efficiency measurements as they are conceptually similar. The spectral response (with units A/W) is a measure of how a device responds to a narrow spectral band of irradiance. It is defined as the ratio of the photocurrent generated by a solar cell under monochromatic illumination of a given wavelength to the value of the spectral irradiance at the same wavelength. In simpler terms quantum efficiency gives the number of electrons output by the solar cell compared to the number of photons incident on the device, while the spectral response is the ratio of the current generated by the solar cell to the power incident on the solar cell. Since the number of photons and irradiance are related, the spectral response can be written in terms of the quantum efficiency as [13]:

$$SR(\lambda) = \frac{q\lambda}{hc} \cdot QE(\lambda) = 0.808 \cdot \lambda \cdot QE(\lambda) \tag{1.1}$$

where,
SR(λ) - Spectral Response of the particular wavelength
h - Planck's constant ($6.625 \times 10^{-34} m^2 kg/s$)
c - speed of light ($3 \times 10^8 m/s$)
q - charge of an electron (1.6×10^{-19} C)
QE(λ) - Quantum Efficiency of the particular wavelength
λ - wavelength (nm)

Ultra-high speed I-V characteristic measurements like Abet 11048 solar simulator, One-sun multisource simulator (OSMSS) etc., are already used in industrial scale production of solar cells [14]. Conventional EQE measurements cannot be used in industrial production environment as the measurement time is generally in the order of a few minutes to get the complete EQE curve for the visible/near-infrared (VIS/NIR) part of the spectrum. This is due to the use of monochromator and lock-in amplifier used in conventional EQE measurements [9] which is discussed in the next section. Fast EQE measurements would thus help in solar cell characterization both in research and industrial scale production.

1.1. Conventional EQE Measurements

This section describes the principle and most important equipment's used in conventional EQE measurements. The bandgap structure of solar cell introduces wavelength dependent absorption of incident light i.e., a photon with energy larger than the bandgap is absorbed by the material, while a photon with energy lesser then the bandgap is not absorbed by the solar cell. The absorbed photon creates an electron-hole pair, which are separated and the recombined through an external circuit. The movement of the electron in the external circuit to recombine with the created hole constitutes current flow. In order to determine the EQE of a device, it is important to know the incident power reaching the solar cell, the current produced by the cell at each wavelength.

1.1.1. Principle of EQE Measurement

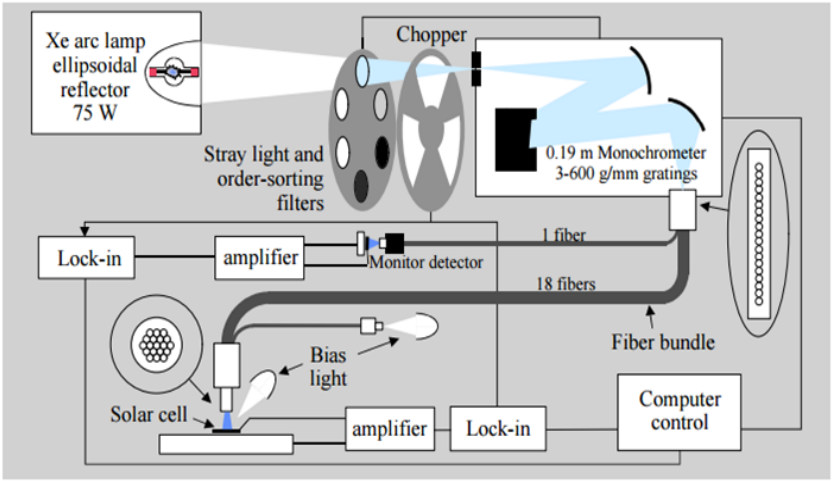

Figure 1.4: Equipment configuration for conventional EQE measurements [15].

A conventional EQE measurement setup consists of a tunable light source, detection system, electrical accessories - current pre-amplifier, lock-in amplifier, optical accessories - filter wheel, chopper, light beam manipulation devices - prism or diffraction gratings etc. The underlying aim of the whole system is to provide a nearly monochromatic light beam to be incident on the test cell with a typical bandpass of 1-10 nm [16], tunable over the entire spectrum over which the solar cell

is active. A computer is used to record the photocurrent produced by the test cell. The power incident is measured with the help of either a calibrated photo diode or a calibrated solar cell. The current produced by the monitoring photodiode or solar cell is also measured simultaneously and the ratio of these two measured current values for each wavelength interval is recorded [15]. Also a correction factor has to be taken into account for the illumination of the monitoring photodiode in this case as the photodiode and the solar cell are illuminated differently (see figure 1.4). The ratio of the current output from the test device to the incident beam power gives the responsivity of the test device, this value is converted to the units of quantum efficiency by using the monochromators wavelength setting. The formula for the same is given below [15]

$$EQE(\lambda) = \frac{100 \times h \times c \times I_{TD}(\lambda)}{q \times I_{ref}(\lambda) \times CV_{ref}(\lambda)} \tag{1.2}$$

where,
h - Planck's constant ($6.625 \times 10^{-34} m^2 kg/s$)
c - speed of light ($3 \times 10^8 m/s$)
$I_{TD}(\lambda)$ - test device current (μA)
q - charge of an electron (1.6×10^{-19} C)
$I_{ref}(\lambda)$ - reference cell current (μA)
$CV_{ref}(\lambda)$ - calibration value of the reference cell (W/A)

1.1.2. Equipment Details

Monochromators

It is the most important component in the conventional EQE measurement setup. The main goal of a monochromator is to provide monochromatic light as output from a white light (polychromatic) source at input. This is achieved by separating and transmitting a narrow portion of the optical signal chosen from a wider range of wavelengths available at the input. The simplest monochromator is composed of two slits (entrance and exit), mirrors (collimating and focusing) and a dispersion element (prism or diffraction grating). Both the dispersive elements take advantage of the dependence of the refraction angle (prism) or the reflection angle (grating) on the wavelength of the incident light. In the case of prism, the larger the photon energy (shorter wavelength) the smaller is the refraction angle, thus bending of light of shorter (violet) wavelengths are different from longer (red) wavelengths. The wavelengths of light coming out of the exit slit can be tuned by the rotation of the dispersing element. The range of wavelengths leaving the exit slit is thus a function of the width of the exit slit.

A basic monochromatic system is shown in the figure 1.5. Light from the source has a spherical wave front (dispersive in nature) and is made to incident onto the collimating mirror (element C) through the entrance slit. The function of the collimating mirror is to reflect the incident light onto the diffraction grating. The collimating mirror also alters the spherical wave front of the incident light to planar or parallel wave front. The diffraction grating has a series of finely etched ridges or grooves which are coated with a highly reflective surface like gold or aluminium, which reflect the light to the focusing mirror (element E) with low absorption losses and high efficiency. The grating reflection process is a combination of constructive and destructive interference patterns of the collimated light. Due to the angle and sharp edges of the diffraction grating, light is reflected at slightly different angles off the grating surface, the white light is separated into its individual components here and the light rays with a planar wave front are incident onto the focusing mirror. The separation of white light into its constituent colors is the heart of the working of a monochromator. This process is called dispersion. Light of different colors and wavelengths which are closely spaced are reflected off the focusing mirror towards the detector via the exit slit. The exit slit is very narrow and only a small wavelength band can be obtained as output onto the detector. The rest of the light is

absorbed by the internal walls of the monochromators which are painted black.

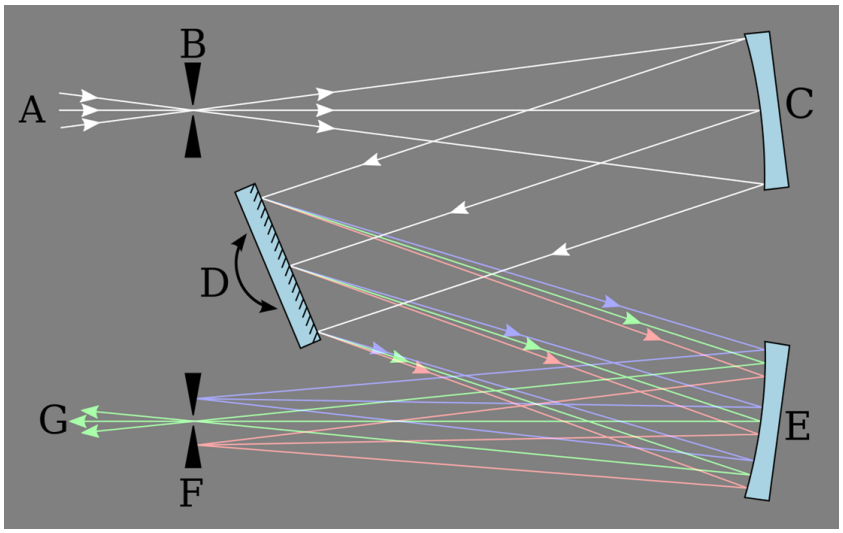

Figure 1.5: Schematic of a basic Czerny-Turner Monochromatic System with A-light source; B - entrance slit; C - collimating mirror; D - dispersive element (Prism or Diffration grating); E - focusing mirror; F - exit slit; G - detector [17].

Light Source

The most commonly used light sources for the monochromator illumination are Mercury arc lamps, deuterium, Tungsten-Halogen (TH) or Xenon (Xe) arc sources. The wavelength range and power throughput needed dictate the choice of light source for the measurements. Deuterium and Mercury arc lamps are ideal sources for applications that require high intensity spectral lines in the deep UV to visible light regions. In a deuterium arc lamp, controlled electric discharge causes D_2 to dissociate and emit light in the spectral range of ± 160 – 400 nm [18]. Further, the unique UV emission spectra of the Mercury arc lamps make them a popular choice for UV spectroscopy, UV curing and other industrial processes.

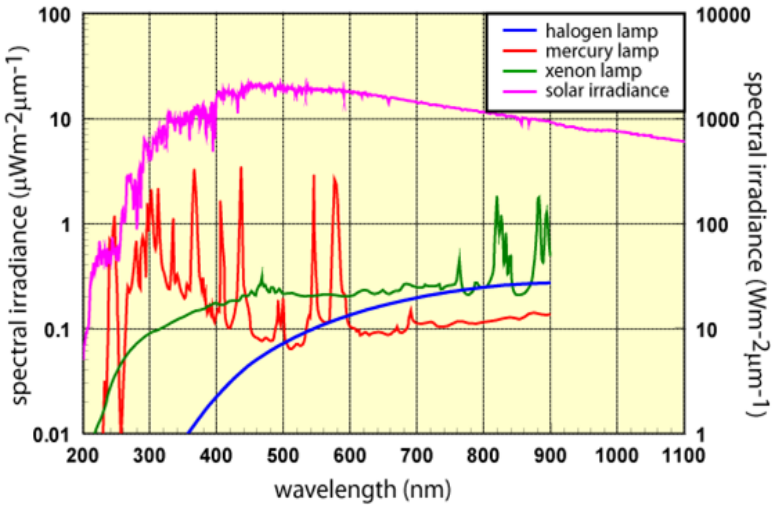

Figure 1.6: Comparison between the spectral irradiance of different artificial light sources (left axis) to the spectral irradiance of the sun (right axis) [19].

Xenon arc lamps are based on the atomic emission spectra of the gas Xenon inside the bulb and emit light in the UV, VIS and NIR spectral range between ± 200 and 2500 nm [18]. Halogen based

light sources emit in a very broad spectral range from visible to infrared between ± 350 and 2600 nm [20]. Tungsten-Halogen lamps are most commonly used light sources for spectroscopy applications as they provide a very smooth and stable spectral output in the range mentioned above [20].

In cases where the light source is needed to cover the UV, VIS and NIR range, hybrid combinations of different light sources can be coupled to the input of the monochromator. Ex – using the deuterium and tungsten-halogen lamp, the whole spectral range from deep UV to NIR (185 to 2500 nm) can be covered [20].

Other Components

The other important equipment's used in the conventional EQE measurement setup shown in figure 1.4, include optical choppers, filter wheels, lock-in amplifier. Optical choppers are rotating discs with mechanical shutters and are widely used in combination with lock-in amplifiers. The chopper is used to modulate the intensity of a light beam. Optical filters or filter wheels are used to selectively transmit light of different wavelengths and are placed in conjunction with choppers after the light source.

In general, any input signal consists of signal and noise. Noise is represented as varying signals at all frequencies. While the signal is present at the defined or reference frequency. Lock-in amplifiers are used to detect, measure and isolate very small AC signals in the range of few nanovolts. An ideal lock-in only responds only to signal at the reference frequency and filters out all the noise by chopping the signal. In EQE measurements the AC component of voltage corresponding to the monochromatic test light is separated from the DC component introduced by bias light. Accurate measurements may be made even when the small signal is obscured by noise many times larger in magnitude than the signal. Lock-in amplifiers use a technique known as phase-sensitive detection to single out the component of the signal at a specific reference frequency and phase. Noise signals, at frequencies other than the reference frequency, are rejected and do not affect the measurement [21].

1.2. Fourier Transform based EQE Measurements

As mentioned earlier, the state-of-the-art conventional EQE measurement systems measure the solar cell's short circuit current for each wavelength of the incident spectrum separately from which the EQE information is gathered. Consequently the total measurement time is directly related to the optical resolution and bandwidth which in most cases is very time consuming [22]. This has been a major road block for the evaluation of homogeneity and reproducibilty of solar cells and modules for both researchers and industrial scale production process. In order to overcome this limitation faster EQE measurement techniques have surfaced in recent times. This section covers the working principles of alternative EQE measurements, their advantages and limitations. Most of these techniques rely on the principles of interferometry to obtain the spectrum of the interferogram which is then analyzed to obtain the final EQE. Michelson interferometer is the most widely used technique in spectroscopy studies and other interferometers (refer to Appendix A.2) have evolved from it. The working principle of Michelsons interferometer is mainly used in Fourier Transform Spectroscopy including Fourier Transform Infrared Spectroscopy (FTIR) and Fourier Transform Photocurrent Spectroscopy (FTPS) etc., the details of which are discussed in section 1.2.3.

1.2.1. Michelson Interferometer

The basic configuration of a Michelson interferometer is shown in figure 1.7. It consists of a light source, a beam splitter, two mirrors (movable and fixed), and a detector used to record the interference pattern. A beam splitter is a half-silvered mirror which is used for dividing the light to be spectrally analysed into two beams with different optical path lengths. One beam passes through the beam splitter to the movable mirror while the other is reflected at 90°, to the fixed mirror as

shown in the figure below. After being reflected by the mirrors, the two beams are recombined by the same beam splitter before finally arriving at the detector. The path difference of the two beams causes a phase difference which results in a signal detected by the detector which is a function of the mirror distance *'d'* called interference fringe pattern. This pattern is detected by the detector and used to evaluate the wave characteristics, material properties or displacement of one of the mirrors.

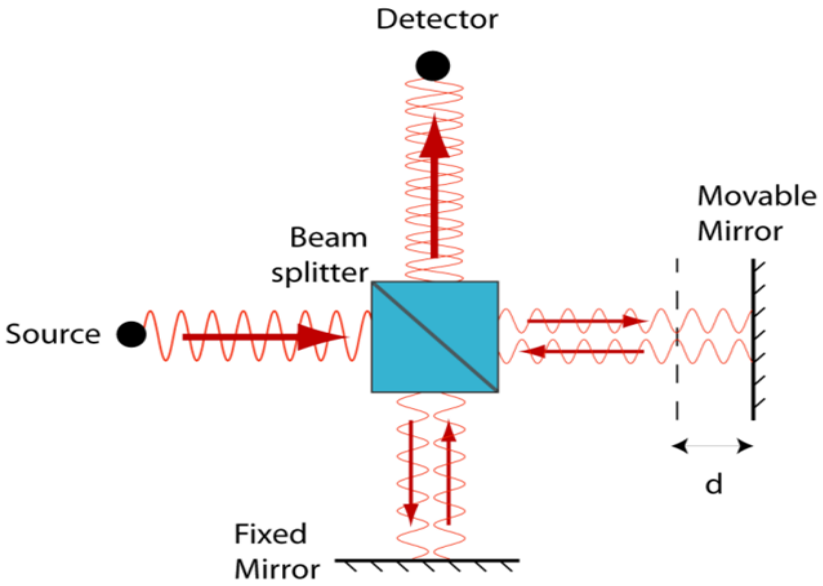

Figure 1.7: Michelson Interferometer Visual Overview - Any small displacement of the movable mirror will lead to path difference between the two beams resulting in an interference pattern on the detector [23].

When the fixed and movable mirrors are equidistant from the beam splitter (d=0) both beams travel the same distance before reaching the detector. However, if the movable mirror is moved away by a distance d, the light beam reflected off the movable mirror has to travel an additional distance $\delta = 2d$ (back and forth). This additional distance is the optical path difference and is called retardation [23].

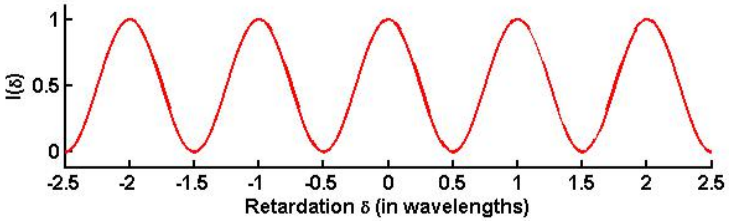

Figure 1.8: Plot of Monochromatic light interferogram generated for different retardations [23].

If $\delta = 0$ (i.e., when the two mirrors are equidistant from the beam splitter) or if δ is an an integer multiple of the wavelength of the incident light ($\delta = n\lambda$, where n is an integer) then the two reflected beams are said to be in phase and they interfere constructively. The intensity at the detector is equal to the intensity of the source. On the other hand, if $\delta = \lambda/2$ or $\delta = (n+1)\lambda/2$, then the two reflected beams are out of phase and they interfere destructively. The intensity at the detector will be zero in this case. For any intermediate retardation's which is possible by changing the position of the movable mirror over a small distance, the intensity recorded on the detector will be a sinusoidal function, which is given by the following equation.

$$I(\delta) = \frac{I_0}{2} \times (1 + \cos\frac{2\pi\delta}{\lambda}) \tag{1.3}$$

where,
I_0 - intensity of the source.

1.2.2. Fourier Transform Spectroscopy

The Fourier Transform Spectroscopy (FTS) is a technique used to measure the spectrum of a substance. It is based on the Fourier pair relationship between the interferogram of a substance and its spectrum [24]. FTS is widely used to measure the spectral transmission, reflection and emission of solids, liquids and gases especially in the infrared and far infrared region of the spectrum [25]. The process of conversion of the interferogram to the spectrum is through the Fast Fourier Transform (FFT) algorithm developed by J.W Cooley and J.W Tukey in 1965 [26].

An interferogram is a plot of the intensity of a signal versus the optical path difference (OPD), hence is a function of time and the output values obtained using an interferogram is in the time domain. The time domain is transformed to frequency domain using the Fourier transforms, which are then deconvoluted to get the spectrum. The Fourier transform of the interferogram can be viewed as the inversion of OPD – wave number (cm^{-1}) as the unit of OPD is *cm*. Thus, in the Fourier transform, a plot of intensity of a signal versus wavenumber is produced.

The recorded interferogram (raw data) is mathematically the sum of all the monochromatic interferograms and can be calculated by using the following equation [24]:

$$I(\delta) = \int_{-\infty}^{\infty} S(\vartheta)\cos(2\pi\vartheta\delta)\,d\vartheta \tag{1.4}$$

where,
S(ϑ) - the spectrum of the light source expressed in wave-number (ϑ)
ϑ - $1/\lambda$ (the inverse of wavelength)

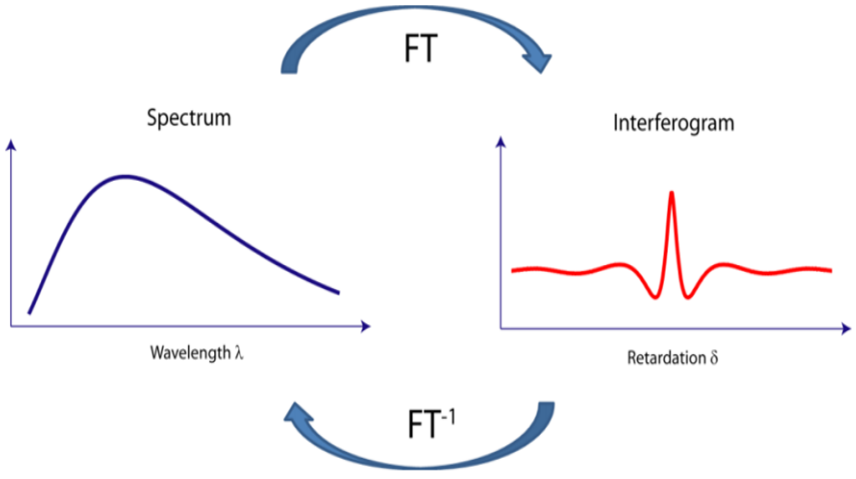

Figure 1.9: Relationship between Spectrum of a light source and Interferogram recorded [23].

The Fourier transform has a simpler mathematical form when expressed in wave-numbers instead of wavelength (λ). The spectrum of the light source producing the interferogram can be ob-

tained using the inverse Fourier transform, that allows calculating the spectrum S(ϑ) from the interferogram I(δ) recorded. The equation for the inverse Fourier transform is given below [24]:

$$S(\vartheta) = \int_{-\infty}^{\infty} I(\delta)\cos(2\pi\vartheta\delta)d\vartheta \tag{1.5}$$

The most important takeaway is that there is a 1-to-1 relation between the spectrum and the interferogram recorded. Each spectrum is related to a unique interferogram and likewise each interferogram corresponds to a unique spectrum. The mathematical relationship between these two can be expressed using the Fourier transform.

With FTS, spectrum of the light source can be recorded much faster with a better Signal-to-Noise (S2N) ratio than using conventional dispersive spectroscopy. The FTS technique also allows for greater sensitivity, hence IR signals below the practical detection limit of dispersive spectroscopy can also be recorded [25].

1.2.3. Fourier Transform Photocurrent Spectroscopy

The Fourier transform photocurrent spectroscopy (FTPS) was initially demonstrated as a fast and sensitive method for the spectral measurement of the absorption coefficient in microcrystalline silicon by Poruba et al [27]. This method enabled very fast measurements of the spectral dependence of the optical absorption co-efficient in thin films of hydrogenated microcrystalline silicon which was generally measured using time consuming techniques like the constant photocurrent method (CPM) or the photo-thermal deflection spectroscopy (PDS).

Hodakova et al. [28], demonstrated quantum efficiency measurements using the FTPS technique. Here the FTPS utilizes the Fourier transform infrared (FTIR) spectrometer as an external light source and as an interferometer and a solar cell connected to an electrical circuit as an external detector (figure 1.10). The electrical circuit consists of a current preamplifier and an analog to digital (ADC) converter which digitizes the current output from the preamplifier. A computer then Fourier transforms this signal from the time domain to the frequency domain. The measured spectrum is then normalized by a spectrally independent or a calibrated detector by taking into account the frequency responses of the device under test and the calibrated detector. It is crucial to use research quality FTIR spectrometers like the Nicolet Nexus 870 [28] in order to obtain the EQE for the range of wavelengths for standard solar cells (400 - 1200 nm) in one run. The different frequency responses of the device under test and calibrated detector are taken into account to determine the final EQE of the solar cell. The measured and normalized FTPS spectrum was found to be in good agreement with the results from conventional QE measurements for both micro-crystalline silicon solar cell (except in the UV region) and a solar sub-cell incorporated in an amorphous silicon mini module when the module terminals were used for connection. The slight mismatch in the UV region was attributed to extremely low intensity of light from the halogen lamp in the spectrometer. Poruba et al. [29] further demonstrated the suitability of the FTPS technique for EQE measurements in micromorph tandem cells and solar cells based on organic bulk heterojunctions as well.

It should be noted that the scanning velocity of the moving mirror used in the FTPS technique causes the photocurrent generated by the solar cell to contain frequency components in low kHz range. This is evident when resolving the response of the solar cell in the VIS/NIR part of the spectrum [9]. This does not pose a problem when conducting FTPS measurements on non-crystalline silicon materials, which have carrier lifetimes in the range 1-10 µs. But this makes it difficult for measurements with time periods exceeding 1 ms. The problem can be circumvented by using lower modulation frequencies but this will result in higher measurement time which is not desirable. However, for c-Si solar cells that exhibit a high absorption like the interdigitated back contact (IBC) solar cells with carrier lifetimes in the range 0.1-10 ms, FTPS technique might not be best

suited. Additionally, an interferometer is a bulky, expensive component and using other techniques to replace the interferometer gained prominence.

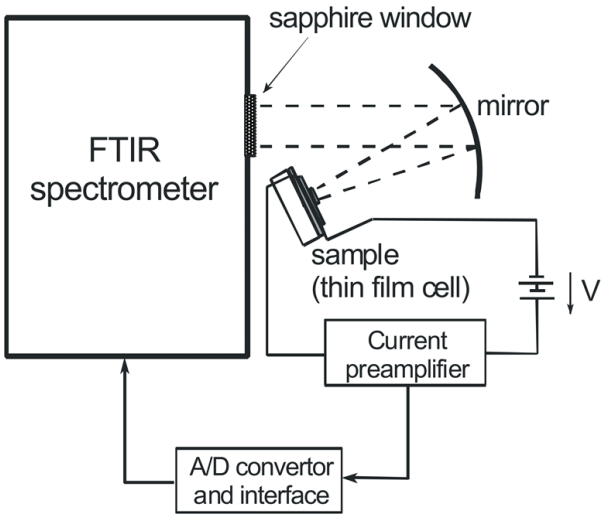

Figure 1.10: Schematic of a Fourier transform photocurrent spectroscopy (FTPS) with a Fourier transform infrared (FTIR) spectrometer for EQE measurements [29].

1.3. LED based EQE Measurements

Light Emitting Diodes (LEDs) as light sources for solar cell measurements have been demonstrated by Klaus et al. [30] as they provide higher illumination intensities and also have higher life times when compared to Xenon or Halogen bulbs. Further the rapid decrease in the prices of LEDs have made it a financially attractive choice for different PV characterisations including EQE measurements. Klaus et al. [30], demonstrated that LED emission can be modelled as a sum of several individual Gaussian profiles to quantify the impact of LEDs on the EQE measurements and have found the deviations from conventional measurements to be 1-2%.

Hamadani et al. [31] further demonstrated different techniques of using LEDs for the determination of spectral response of a solar cell. The first method was based on an individual LED lock-in technique (similar to the one used in conventional EQE measurements) and the other based on synchronous multi-frequency optical excitation using the Fourier transform technique. This was achieved using a wide variety of LEDs of different wavelengths to construct a spectrally tunable source as shown in figure 1.11. All the LEDs are powered by computer controlled LED drivers. The entire EQE measurement is performed by sequentially pulsing each of the 32 LEDs and the photocurrent generated by calibrated cell and the device under test is measured. The ratio of the two quantities will yield the EQE of the device under test. The entire measurement took about 5 minutes.

In the second technique all 32 LEDs are powered at the same time by the LED drivers but with slightly different frequencies. The time-dependent photocurrent signal generated in the solar cell as a result of these pulsed illuminations are detected by a signal analyzer in the frequency domain. In this measurement too, a calibrated reference Si diode is placed under the same illumination in order to obtain the optical flux at each LED wavelength, then, the diode is replaced by the device under test (solar cell). The ratio of inverse Fourier transform of the photocurrent signals will provide the spectral response of the cell across the wavelengths of the LEDs in close to 5 seconds. The LED based spectral response data showed good agreement when compared with the conventional EQE measurements. Further the lock-in technique provided more accurate measurements compared to the Fourier transform technique.

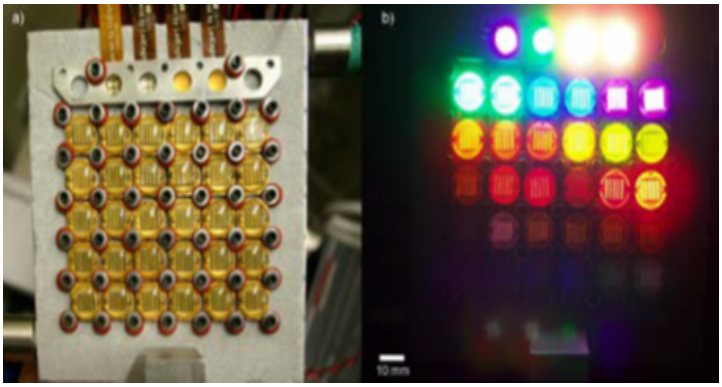

Figure 1.11: a) LED matrix constructed using 30 LEDs to simulate a spectrally tunable light source. Additional 2 high power white LEDs (mounted on the plate's top edge) were used as light bias. b) The LED matrix under operation. The LEDs on the second row from bottom emit radiation in the NIR spectrum, hence appear faint. The bottom row of LEDs emit radiation in the IR and hence are invisible to the human eye [31].

The time advantage gained in LEDs is often downsided by the loss of flexibility, bandwidth and optical resolution and spectrum wider than 1000 nm for which commercial LEDs are a rarity [22]. Further the commercial non-availability of LEDs in the UV and far IR region limits their usage in EQE measurements to the wavelength range 300-800 nm [32].

1.4. Fast Optical Measurement System

This section explores the working principle of an alternative novel EQE measurement system called the Fast Optical Measurement System (FOMS). A prototype was developed by the Delft Spectral Technologies team (DST) that can measure the EQE of a crystalline silicon solar cell in the VIS/NIR range of the spectrum within a measurement time of 1-10 seconds. This is made possible using the advances in micro-opto-electromechanics (MOEMS) and the computational power of computers. The heart of the system is a spatial light modulating element called Digital Micromirror Device (DMD) developed by Texas Instruments.

1.4.1. DMD Working

The DMD is both a micro-electronic mechanical system (MEMS) as well as spatial light modulator (SLM). It is a MEMS device as it consists of hundreds of arrays of moving micromirrors that are controlled by the underlying CMOS memory unit [33]. A DMD consists of orthogonal arrays of highly reflective aluminum micromirrors (also called pixels). These micromirrors have a tilt angle of $\pm$ 12 °, which is used to control or direct the light reflecting off the DMD on the device under test (figure 1.13). By convention the positive (+) state is tilted toward the illumination of the cell and is referred to as "ON" state and the negative (-) state is tilted away from the illumination of the cell and it referred to as "OFF" state. The figure 1.12, shows two pixels (micromirrors), one in the "ON" and other in the "OFF" state, the only two operational states of the micromirror. The micromirrors are attached to the DMD by means of a torsional hinge on the underside of the micromirrors which make contact with spring tips and an integrated circuit chip [34]. The alignment of the micromirrors is controlled by the influence of an electrostatic field.

The different components making up an indivudual pixel can be seen in figure 1.14. Underneath each micromirror is an integrated memory circuit consisting of dual complimentary metal-oxide semiconductor (CMOS) memory shown in figure 1.15. The state of the two memory elements are complementary, i.e., if one element is in the logical 1 state, then the other is in the logical 0 state. In order for the state of the CMOS memory to be transferred to the mechanical position of the micromirror, the pixel must receive a "mirror clocking pulse" (a reset trigger). This pulse will

momentarily release the micromirror from its existing state and realigns it based on the state of the CMOS memory underneath. It is therefore crucial that the memory cell is not overwritten during a mirror clocking pulse operation. Hence, based on the image (binary frame) mounted on the DMD memory, the mirrors align accordingly [35].

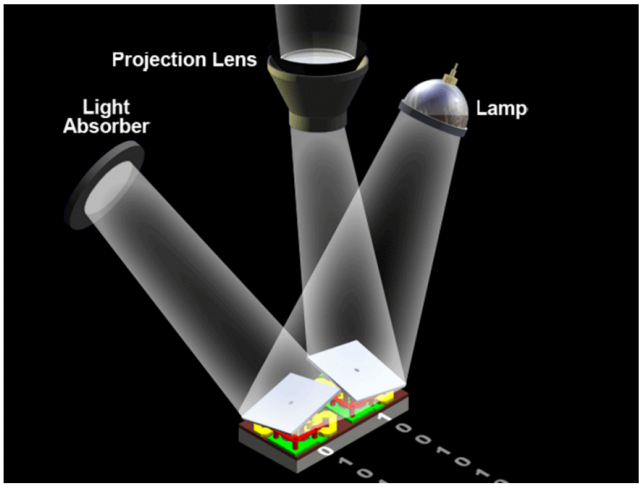

Figure 1.12: The two operational states of micromirrors. The logic states 0 and 1 represents the OFF and ON state of the micromirror respectively [35].

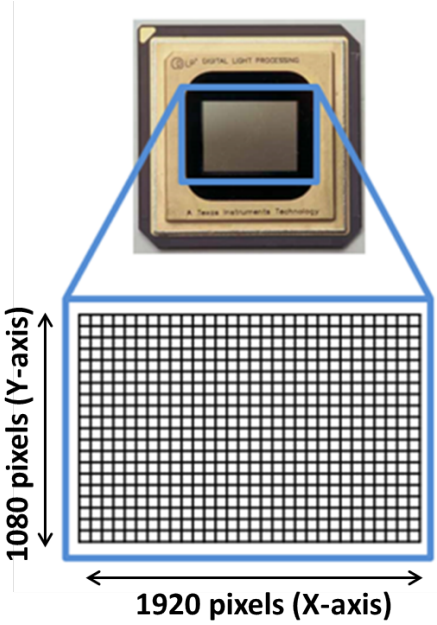

Figure 1.13: Schematic of a full HD DMD chip with 1080 pixels (Rows) × 1920 pixels (Columns) used as the light modulation device in the Fast Optical Measurement System.

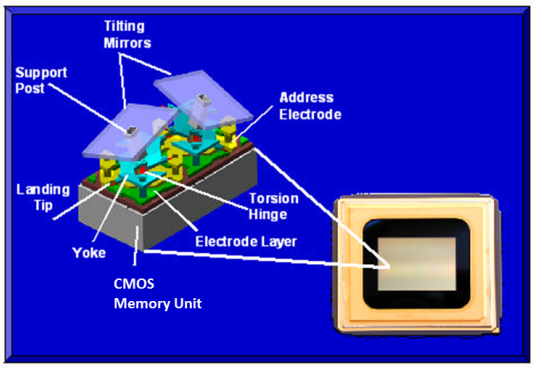

Figure 1.14: Different components that control the tilt of DMD micromirrors [35].

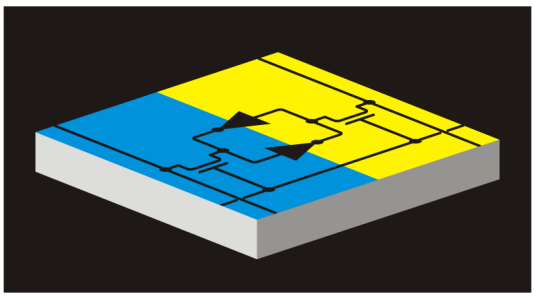

Figure 1.15: The Dual CMOS Memory used to control the operational states of the micromirrors on the DMD [35].

Additionally the DMD is used in Advanced Light Control Digital Light Processing products for high speed industrial, medical and advanced display applications [35]. The DMD chips have a higher refresh rates when compared to the liquid crystal displays (LCDs) which are another alternative, but the DMD chips are mass-produced, cost effective and the hardware control with data processing abilities is well known in the projector markets. Hence making it an ideal choice to substitute interferometers in EQE measurements [9]. Using the power of a DMD chip as a light modulation device, the Fast Optical Measurement System was developed by the DST Team and the resulting

EQE curves obtained using this system was in close conformance to the EQE curves obtained using the conventional monochromatic EQE system, hence making it a viable alternative.

1.4.2. Working of FOMS

The working principle of FOMS system can be described with the aid of figure 1.16. Polychromatic white light from a halogen lamp is made to fall on a dispersive element through a slit and filter wheel. The dispersive element, a flat field corrected image grating splits the polychromatic light, and the dispersed light is projected onto the DMD chip. The DMD chip acts as a spatial light modulator producing two light beams, one of which is incident on the solar cell under test via focusing optics as shown in the figure 1.16. The other beam from the DMD is lost (unused) currently, but there are plans to incident this beam onto the reference detector, which will enable simultaneous measurements of both the device under test and the reference cell.

The halogen lamp is used as the light source because the emission spectrum from a halogen lamp is smooth, without peaked features as observed in the emission spectrum of a Xenon lamp in figure 1.6. This is particularly useful in EQE measurements as the need to suppress the sharp spectral peaks that might otherwise be present in the EQE measurement data can be eliminated.

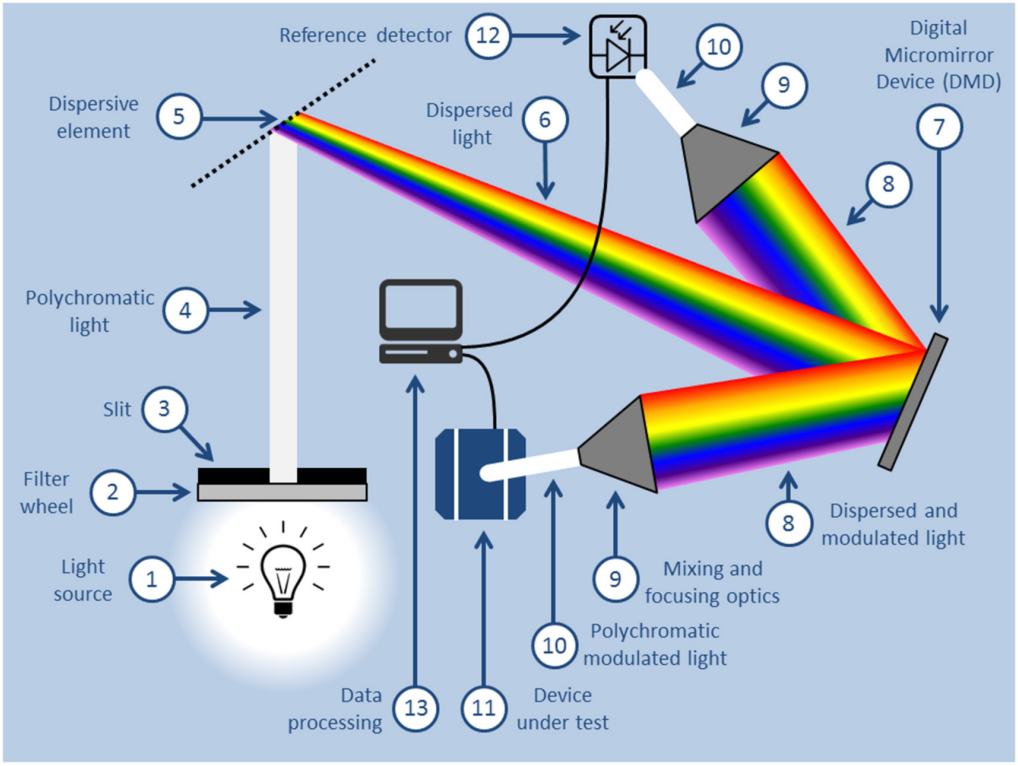

Figure 1.16: Schematic Layout illustrating the working of Fast Optical Measurement System [9].

To understand the EQE measurements with the FOMS setup it is important to understand the working of the DMD chip in this setup. As mentioned earlier the dispersed light from the grating is projected onto the DMD chip which consists of a certain number of mirrors arranged in rows and columns as shown in figure 1.13. The spectrum projected on the DMD aligns along the columns and rows such that, each column of the mirror corresponds to a certain wavelength and thus a corresponding modulation frequency. As the mirrors on the DMD chip can be individually controlled between the ON state and OFF state by pivoting about an axis, this enables controlling the intensity of the light beam for each wavelength of the projected spectrum.

The motion of the moving mirror in the Michelson interferometer used in FTPS is mimicked

in this system by projecting a set of bitmap images which are developed using MATLAB. By projecting a sequence of images onto the DMD over time, different modulation frequencies result for different projected wavelengths (see figure 1.17). These images are mounted on the controller of the DMD which is in turn connected to a computer and the images are sequentially loaded onto the DMD with the help of the CMOS memory unit and the computer. The mirrors on the DMD switch between ON and OFF state based on the image on the DMD and this results in modulation of the incident light. The modulated spectrum components are subsequently recombined to polychromatic white light and incident on the solar cell under test with the aid of focusing lens and integrating rod to collect all the light deflected off the DMD. The resulting currents from the solar cells (both the calibrated device and the device under test represented by 11 in figure 1.16) is then amplified and converted to their voltage equivalents by means of a transimpedance amplifier and then digitized using an Analog-to-digital (ADC) converter. This modulated current signal is then recorded using a computer.

As the current signal generated from both the calibrated cell and the device under test contain the spectral responsivity information, they need further computation. Since the modulation scheme used here is similar to the one used in FTPS, the measured photocurrent from both the calibrated device and device under test will be modulated in the same fashion. The digitized measurement data from both the calibrated solar cell and the device under test are then post-processed using inverse Fourier transforms, and the final EQE of the device under test is the ratio of the two signals.

The major improvement of the FOMS prototype over the FTPS is the dependence of measurement time on controllable variables. In the FTPS setup the modulation frequency and measurement time are connected to the velocity of the moving mirror of the interferometer, while in the FOMS setup the measurement time is determined by the display time of a single image on the DMD and the number of images projected onto the DMD. Both these variables can be independently controlled using a computer in FOMS which is not possible in the FTPS setup. Hence the resolution in the FOMS is not dictated by the velocity of the moving mirror but by the ratio of retardation, i.e. the displacement of the simulated moving mirror and the number of images that are projected onto the DMD. The ratio has been optimized such that the data points in the final EQE curve are spaced about 5 – 15 nm apart [9], which is also the typical wavelength resolution in a monochromatic EQE measurement. Further this system is functional for a larger wavelength ranges extending to far IR regions of the spectrum as well, which is a limitation in the LED based EQE measurement systems.

1.5. Aim and Outline of the Thesis

The FOMS prototype as mentioned earlier works on the Michelson interferometer based modulation scheme. The limiting factor to expand FOMS setup's versatility and utility lies in its inability to work with other modulation scheme. The changes that needs to be done to test other promising modulation schemes (see section B) is cumbersome on the actual setup and hence a model to mimic the working of the FOMS prototype is helpful. The model can act as an useful tool to test and validate different modulation schemes and the promising ones can then be transferred to the actual setup. The model also helps eliminate unnecessary complexities in the hardware and software changes of the actual setup. More information on the need for the model is detailed in section 3.1 of Chapter 3.

The objective of this thesis is to investigate, characterize and model a promising fast EQE measurement technique called Fast Optical Measurement System (FOMS) developed by Delft Spectral Technologies (DST) team. The model needs to simulate the working of the FOMS system and this will be validated. In view of the above, the main research question of this work is:

To investigate, characterize and model a promising fast EQE measurement technique called Fast Optical Measurement System developed by Delft Spectral Technologies team.

The following sub-tasks have been defined to complement the above research objective:

1. Characterize the FOMS prototype by determining the optical losses, spectral distribution and intensity variation on the DMD.

2. Develop a model that simulates the working of the FOMS prototype by using the characterization results.

3. Validate the developed model by using a modulation scheme.

This document is structured in the following way : Chapter 2 deals with the characterization of the optical system of the FOMS. The different measurements performed in the characterization step, the need for the different experiments and their results will be explained in this chapter. Chapter 3 describes the development of a model to simulate the working of the FOMS. The need for this model and the different sub-functions developed to build this model is described in detail. The subsequent chapter details the validation of the model using a new modulation scheme. The current output from the model and the FOMS prototype when an image sequence corresponding to a modulation scheme is loaded is detailed. Results from different configuration of the modulation scheme are also explained. Finally, chapter 5 presents the conclusions and future recommendations where the most important results that were obtained during the course of this thesis are recapped.

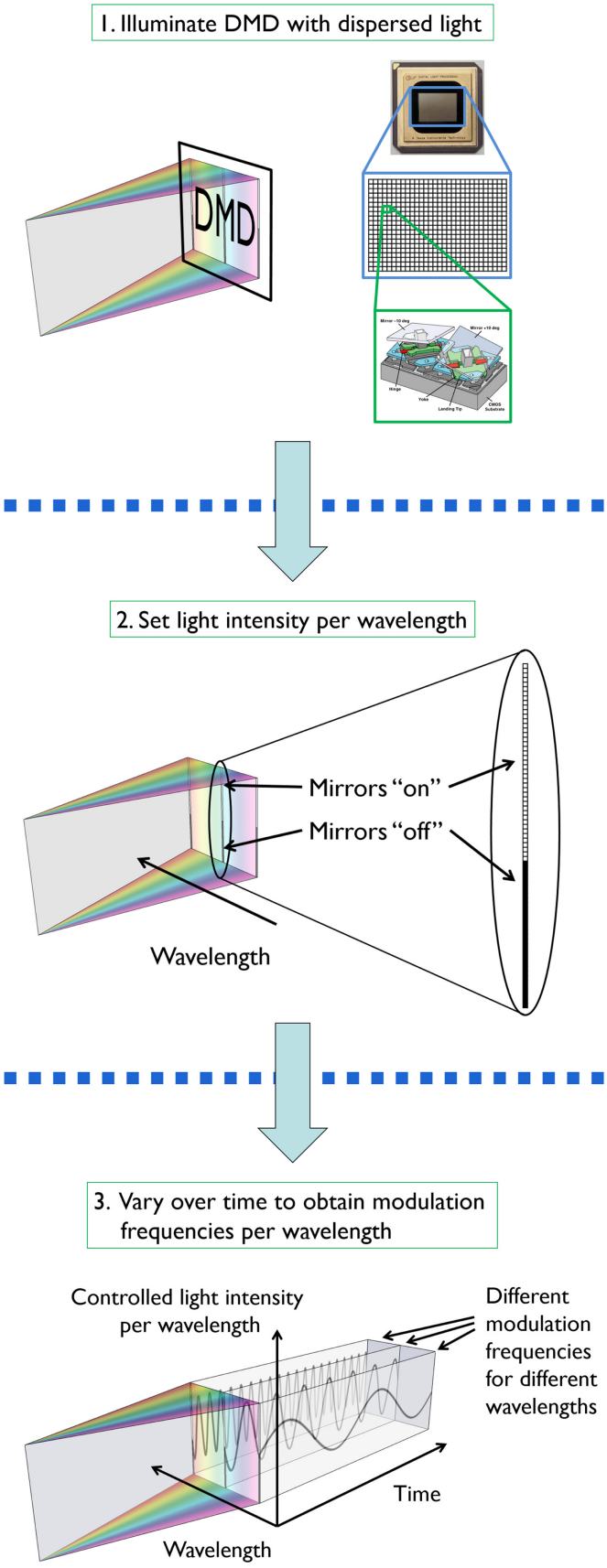

Figure 1.17: Schematic visualization of light modulation using a DMD chip [9].

2

Characterization of the FOMS Optical System

The aim of this chapter is to characterize the optical system of the Fast Optical Measurement system (FOMS). This chapter details the different experiments performed to determine the optical losses, spectral distribution and intensity variation on the DMD and the optimization of the optical path. It should be noted that these experiments relating to the characterization of the optical system have not been performed earlier by the DST team and hence will aid in better understanding of the FOMS model. Also to be taken into account, the words micromirror and pixel will be interchangeably used in the subsequent sections as they mean the same in the context of the DMD.

A few assumptions listed below were made by the Delft Spectral Technologies (DST) team while developing the current modulation scheme (based on Michelson interferometer) for the FOMS prototype. These assumptions will be validated in this chapter as well.

- The first assumption relates to the spectral distribution of the projected light on the DMD. The spectral width which is the number of pixel columns occupied by one wavelength interval was assumed to be constant along the 1920 micromirrors (X-direction) of the DMD.
- The second assumption relates to the intensity variation on the DMD. The intensity of the projected spectrum onto the DMD was assumed to be the identical along a column of micromirrors (1080 micromirrors in the Y-direction).
- The third assumption relates to the wavelength curvature of the projected spectrum. It was assumed that all the micromirrors along a pixel column on the DMD (1080 micromirrors in the Y-direction) has the same central wavelength projected on them.

2.1. Calculation of Optical Losses

The initial step carried out in characterizing the optical system was to determine the optical losses of the prototype. The light throughput efficiency which indicates the fraction of the incident light that is available at the output is necessary to evaluate the optical losses. The optical losses were thus determined between the entrance slit (denoted as 3 in figure 1.16) and the exit of the setup (denoted as 10 in figure 1.16). Since determining the optical losses at each of the optical components in the setup is a time consuming process, the overall throughput efficiency was calculated for the incident light.

The optical losses were evaluated with the help of spectrum recorded using the Avantes spectrometer. The spectrum of the light source after the entrance slit is shown in figure 2.1. The intensity

of the incident spectrum is very low in the UV region and gradually increases in the VIS region before reaching a peak at around 850 nm and thereafter starts to drop beyond 900 nm (IR region). This trend is in accordance with the spectrum of a general tungsten-halogen bulb shown by the blue curve in figure 1.6. It should be noted that the spectrum of a halogen bulb is much smoother than the one shown in figure 2.1. The sharp spikes in the plot could be due to the calibration error of the spectrometer. Generally the spectrometer is calibrated with a much lower intensity light source and exposing the spectrometer to a high intensity source after the entrance slit in this case could result in higher discrepancies.

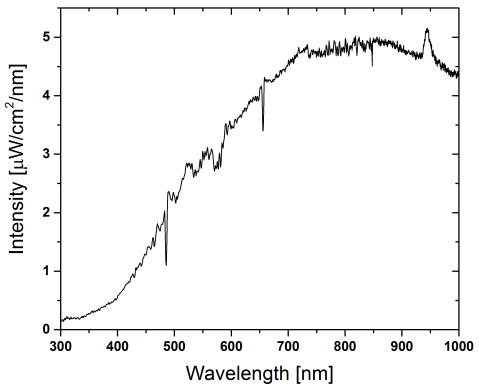

Figure 2.1: Incident Halogen bulb Spectrum recorded after the entrance slit. The sharp spikes in the spectrometer plot could be a result of calibration error of the spectrometer.

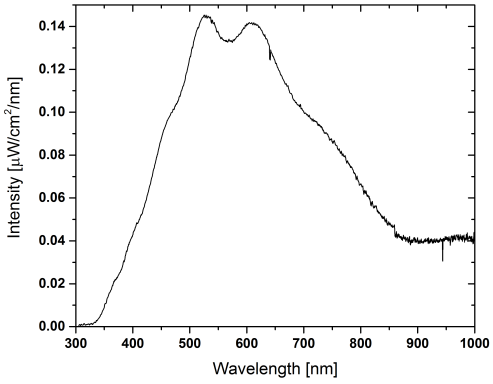

Figure 2.2: The spectrum of light deflected off the DMD recorded at the exit of the optical setup. The reason for the noise in the plot beyond 900 nm wavelength is due to the poor responsivity of the spectrometer in the IR region of the spectrum.

The spectrum at the exit of the setup after traversing through the optical components like lenses, mirrors, diffraction grating, DMD etc is shown in figure 2.2. As the halogen bulb has a much lower intensity at the exit of the spectrum and the spectrometer has better responsivity for low light intensities, this curve is much smoother when compared to the incident spectrum after the entrance slit shown in figure 2.1. It should be noted that in order to deflect all the light projected on the DMD onto the spectrometer all the micromirrors on the DMD were turned ON. The spectrum at the exit, has a very low intensity in the UV region, increases moving into the VIS region reaching a peak at around 550 nm and thereafter decreases into the IR region. On comparing the figures 2.1 and 2.2, it can be seen that the light throughput in the UV and IR regions of the spectrum is the least around 1% and around 4% in the VIS region. Hence most of the incident light is lost in the interim and does not reach the solar cell, placed at the exit of the setup. The major reasons for the losses could be the poor efficiency of the flat field diffraction grating, losses due to the absorption and reflection of light by the various optical components used in the setup. Also overfilling the DMD along the Y-axis in order for the light to be projected across all the 1080 micromirrors in the Y-direction, could result in optical losses. Also, some amount of light could be lost owing to the front surface reflection of the DMD micromirrors and along the edges of the individual DMD micromirrors as they are not edge-to-edge connected.

2.2. Optical Path Optimization

In the course of performing the spectral distribution experiments to determine the spectral width of the projected light on the DMD which is discussed in section 2.3.1, it was noticed that the entire spectrum from the halogen light source was not projected on the DMD. It was observed that the

VIS region of the spectrum started from pixel column number 50 of the DMD, thereby making it uncertain if the whole UV region was being projected on the DMD. In order to verify the same, the current output of a calibrated solar cell in the existing optical path was measured to be 93 μA. Then different optical components were adjusted and maneuvered in order to check if the current output from the cell increased. An increase in the cell current would mean more light being incident on the solar cell, thus making our hypothesis that a part of the spectrum to be missing be valid. The realignments of the optical components were done by adjusting the heights of the mounting poles, by tilting the mirrors and lenses to different angles etc. Since light in the UV and IR regions cannot be seen by the naked eye and different permutations and combinations were done for this sake, and for each of the configuration the current output from the calibrated solar cell was measured. The maximum current output from the solar cell increased by 18% to 110 μA for one such configurations as shown below in the figure 2.3. This increase in current is significant, as was seen in section 2.1, there is a huge reduction in the throughput of light when compared to incident intensity. Thus any increase in current is beneficial and also the part of the spectrum that was missing in the earlier optical path is now projected on the DMD. This was thus fixed as the optimal optical path and all the readings or measurements henceforth are based on this realigned path.

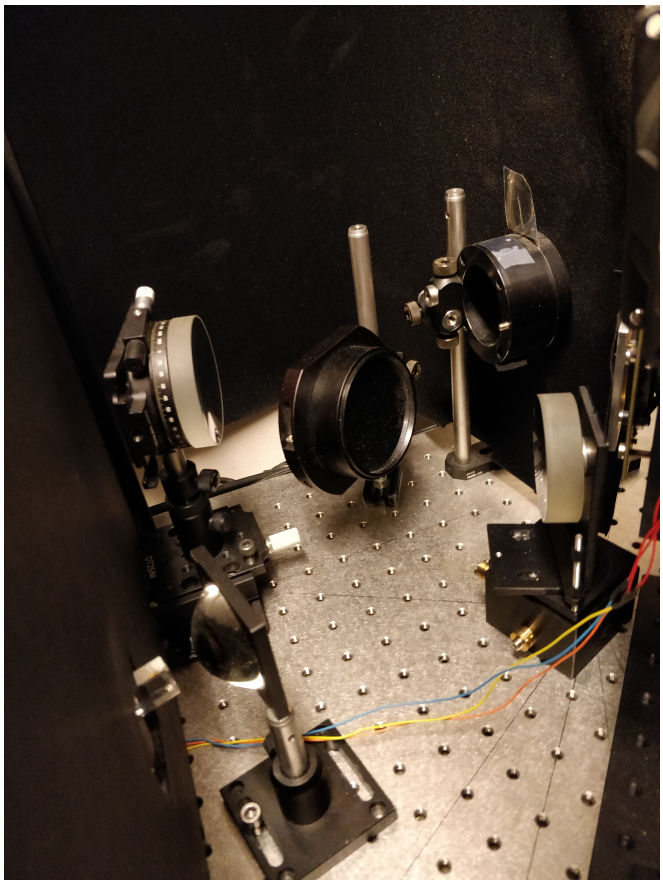

Figure 2.3: Final optimized optical path of the FOMS prototype. An 18% current increase was observed on a solar cell due to the optical path optimization.

2.3. Spectral Distribution on the DMD

Prior to doing the experiments in this section there may be unknown wavelength positions, wavelength distortion and rotation of the DMD from the optical plane and to establish these, the characterization step is needed. There are two measurements done for the characterization of the optical

system - Spectrometer measurements done with the aid of an Avantes Spectrometer and Current measurement done with a high resolution ammeter (nano-Ampere range) 2.3.3. The spectrometer measurements have a spectrometer at the end of the setup and the current measurements have a solar cell (calibrated device) at the exit of the setup.

In the spectral distribution measurements to follow, a line scan pattern as shown in figure 2.4 was used to control the light projected on the DMD. The scans were made across the DMD using small rectangular blocks in order to determine the spectral width and spectral spread. To enable this bitmap images of dimensions 1080×1920 pixels (1080 rows and 1920 columns) were developed and small white rectangular regions of the desired dimensions according to the experiment conducted were created using MATLAB. These images when loaded on the DMD can be used to control the ON and OFF of the DMD micromirrors (as explained in section 1.4.2) and this block of pixels was shifted across the DMD in small increments as shown in the figure 2.4.

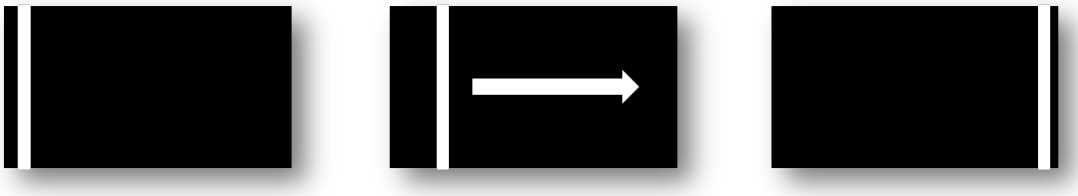

Figure 2.4: Bitmap images of dimensions 1920 pixels (X-direction)×1080 pixels (Y-direction) with line scan pattern - the white rectangular block suggests ON micromirrors on the DMD, the rest of the micromirrors are turned OFF.

2.3.1. Spectral Width Determination

Light after getting diffracted from the flat field corrected diffraction grating splits into its constituent wavelengths and falls along the 1920 pixel columns on the DMD. The experiments performed in this section will deal with determining the Spectral Width which is defined as the number of pixels columns along the X-direction of a DMD that a single wavelength interval would occupy when projected on the DMD. This was done using the spectrometer and bitmap images in a line scan pattern shown in the figure 2.4. Further these measurements will also enable ascertain the central wavelength corresponding to different pixel columns on the DMD. It should be noted that the width of this rectangular region has to be narrow enough to get accurate peak locations of the wavelength intervals, but should be wide enough to get enough signal, to distinguish it from noise. This was achieved by changing the column width (iteratively) in different regions of the spectrum. Scanning this pattern across the DMD yields the specifics related to peak or central wavelengths in the spectrum to the corresponding pixel columns on the DMD. This is due to a 1-to-1 correspondence between the pixel column number and the wavelength interval for that particular rectangular block. This provided the calibration correlation between the wavelengths of the spectrum and the corresponding pixel column on the DMD.

Due to technical limitations of the spectrometer, in obtaining individual wavelength intervals to be projected on the DMD, the wavelength intervals projected on the DMD when a few columns of pixels on the DMD are turned ON is determined. Also due to time limitations in detecting the spectral width for every wavelength interval in the spectrum, the average spectral width across the 3 regions of interest in the spectrum – UV (350 to 400 nm), VIS (401 to 700 nm) and IR (701 to 1050 nm) were determined. Using the line scan pattern described above (figure 2.4), a set of pixel columns on the DMD were turned ON and the resulting spectrum reflected off the DMD was captured using a spectrometer. This was followed for the three regions of the spectrum and the readings were used to get the average number of pixels that every nm of light in the spectrum occupies on the DMD. The

spectral width was calculated on the basis of Full Width Half Maximum (FWHM), to enable easier comparison across the different regions of the spectrum.

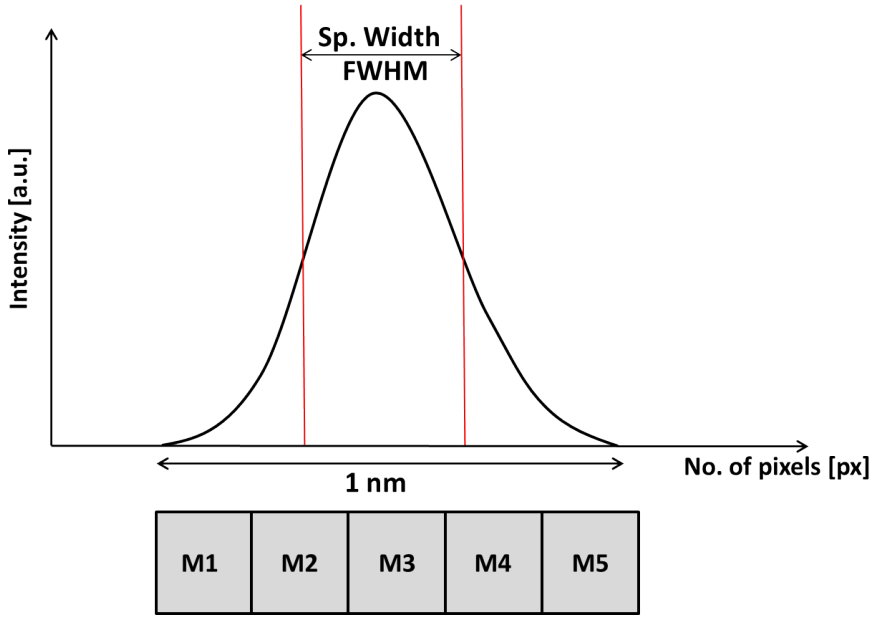

Figure 2.5: Schematic representing the concept of spectral width. The spectral width is measured in terms of FWHM for easier comparison across the regions. In the above figure, the spectral width is around 2 pixels/nm.

(a) Bitmap image with columns 651 to 685 turned to logical state 1, which corresponds to ON state of the DMD

(b) Bitmap image with columns 1041 to 1090 turned to logical state 1, which corresponds to ON state of the DMD

Figure 2.6: Sample Bitmap images used for determining the spectral width. Figures 2.6a and 2.6b corresponds to the VIS and IR region of the spectrum respectively. Since the responsivity of the spectrometer is better in the VIS region, figure 2.6a has a narrower white rectangular block than figure 2.6b.

Figure 2.7, shows the spectrometer plot when the pixel columns 651-685 are turned on which corresponds to the bitmap image shown in figure 2.6a. This pixel column range belongs to the VIS region of the spectrum with a FWHM of 15 nm in the wavelength range 524-539 nm. Figure 2.6b, shows the pixels columns 1041-1090 switched ON. The spectrometer plot when this image is loaded on the DMD is shown in figure 2.8, where the FWHM of the spectrum corresponding to this image is 21 nm in the wavelength range 703-724 nm which lie in the IR region of the spectrum. By dividing the number of pixel columns to the FWHM of the wavelength intervals, an approximate measure of the number of pixel columns needed for every wavelength interval can be obtained. All the readings are measured with FWHM of the interval range as the base.

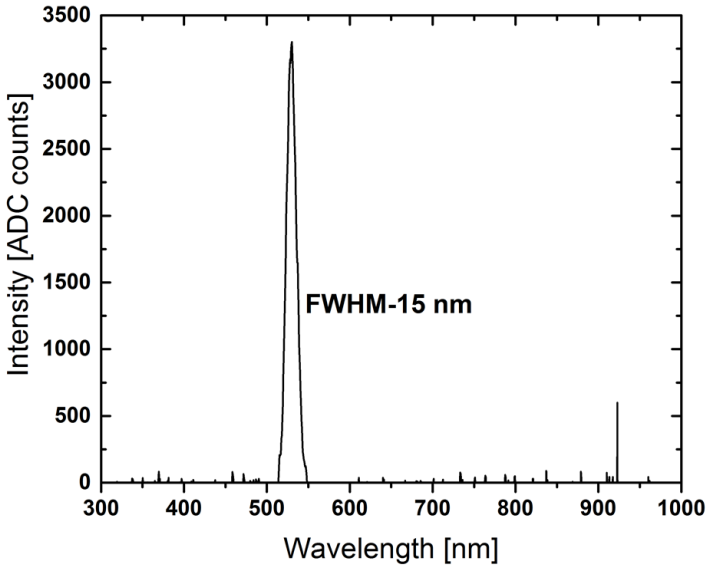

Figure 2.7: Spectrometer plot when mirrors 651 to 685 (figure 2.6a) are turned ON on the DMD. The spectral width based on FWHM in the visible region is around 2.24 px/nm.

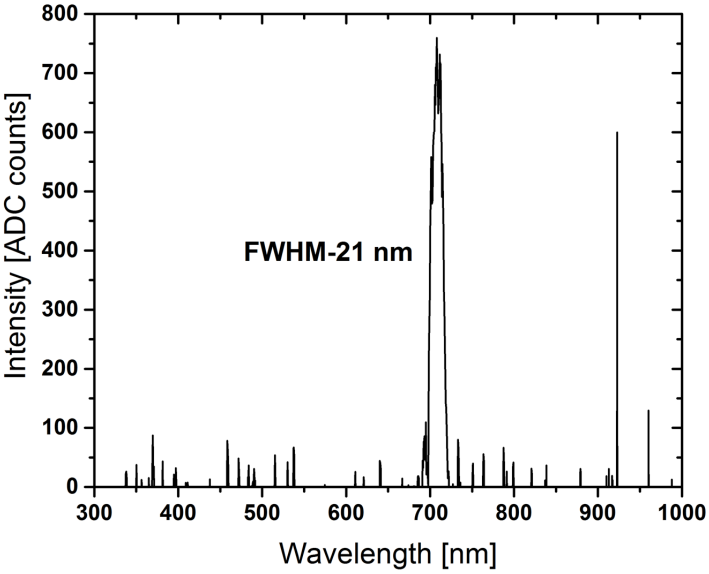

Figure 2.8: Spectrometer plot when mirrors 1041 to 1090 (figure 2.6b) are turned ON on the DMD. The spectral width based on FWHM in the infrared region of the spectrum is around 2.32 px/nm.

By determining the spectrometer plots generated by the line scan pattern using bitmap images across the length of the DMD, the average spectral widths across the three regions of the spectrum, i.e., UV, VIS and IR were found to be 2.11 pixels/nm, 2.24 pixels/nm and 2.32 pixels/nm respectively. A possible reason for this trend could be the optical alignment of the DMD with respect to the diffraction grating. If the optical plane of the DMD is parallel to the optical plane of the flat field diffraction grating, then the spectral width will be almost equal across the spectrum. On the other hand if the optical plane is shifted by any angle, as shown in figure 2.9, then the spectral width of wavelengths can be expected to increase from UV to the IR region as the light in the IR region has to travel an extra distance when compared to the light in the UV region to be projected on the DMD.

The variation in the spectral width across the three regions essentially means that the photon

flux corresponding to a particular wavelength interval in the spectrum is not projected on just one column of pixels, but is spread across a few columns depending on the region where the wavelength interval lies. Thus the calculation of the photon flux for a pixel column will have to take the spectral width for each region into account. Also the calculation of the final current output from the FOMS will have an influence which is discussed further in section 3.4.

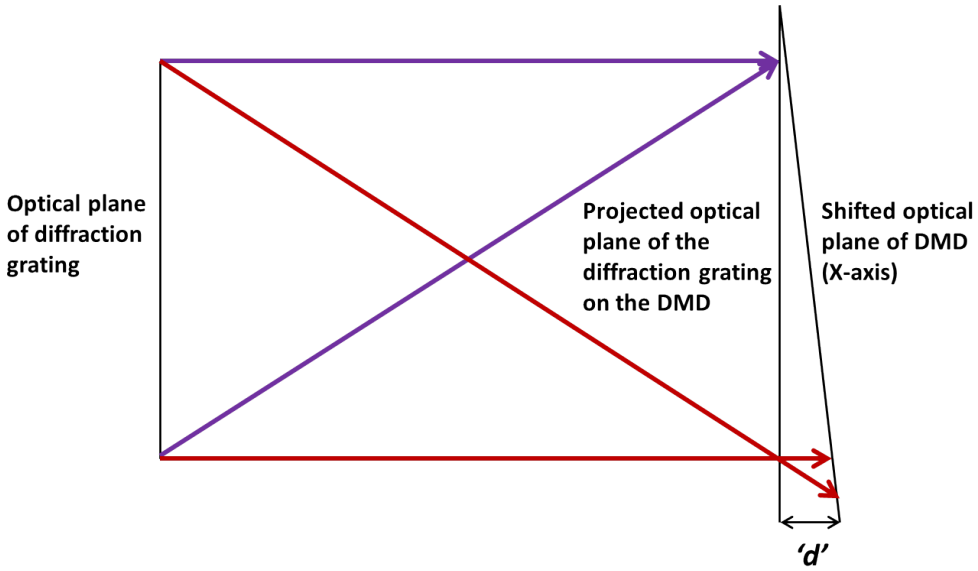

Figure 2.9: Illustration showing the shift in optical plane of DMD. This shift in the optical plane of the DMD can be due to improper mounting of the DMD or mechanical movement of the DMD under the influence of other external parameters.

Additionally the spectral width measurements also provided an approximate outlook on the central wavelength for different pixel columns on the DMD. For instance, from figure 2.6a we can estimate that that centre of this pixel column range (668th pixel column) will have a central wavelength (531 nm) corresponding to the spectrometer plot in figure 2.7 with the FWHM ranging from 531 to 539 nm. Similarly for figure 2.6b, the central wavelength for the pixel column 1065 will be around 712 nm from its respective spectrometer plot (figure 2.8). Also, by varying the width of the rectangular white block in the bitmap images and discerning the spectrometer plots for each of them, the above mentioned central wavelength based estimates were reevaluated. By scanning the rectangular white block over all the 1920 pixel columns of the DMD, a fairly good estimate of the shift in the central wavelength for different pixel column ranges was made. It should be noted that, this hypothesis was further validated in the measurements performed in sections corresponding to Spectral Spread (section 2.3.2) and wavelength curvature determination that are discussed subsequently. Using the data from all these measurements a rough estimate could be made about the central wavelengths corresponding to different pixel columns on the DMD. Further details about this mapping is discussed in Chapter 3, section 3.2.

2.3.2. Spectral Spread Determination

The experiments conducted in this subsection follows up from the experiments done in 2.3.1. To understand the concept of Spectral Spread, the concept of Spectral width discussed earlier needs to be revisited. Consider the spectral width in the UV region which is 2.11 px/nm. This essentially means that the FWHM for one nm of wavelength in the UV region will be projected across 2.11 pixels on the DMD. For illustration, consider a 355 nm wavelength (in the UV region), when projected on the DMD occupy the pixel column range 303 to 305. Now when the pixel column 305 is considered,

it will have a central wavelength of its own and also the influence of the 355 nm wavelength. Thus in this manner, every pixel column on the DMD can have influence of more than one wavelength, on either side of its corresponding central wavelength and this is termed as Spectral Spread.

The concept of spectral spread can be understood better with the illustration shown in figure 2.10. Consider the rectangular block shown to be equivalent to a single pixel column with 1080 micromirrors. The spectrum recorded across this pixel column when measured using a spectrometer shows the influence of a few nanometers of light over the single pixel column. As all the pixels in the pixel column lie along a straight line, the influence over a single pixel in the pixel column is assumed to be the same as that over the pixel column. The spectral spread is thus defined as the number of wavelengths having an influence on a single pixel column on the DMD when light is projected on it. The measurements to follow is an attempt to determine the spectral spread across different regions of the spectrum.

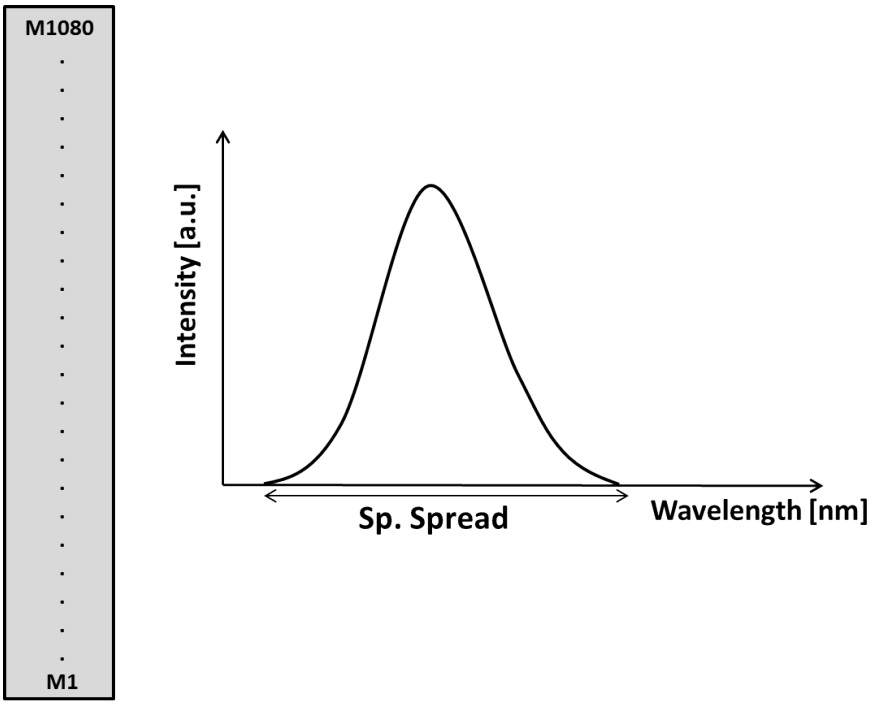

Figure 2.10: Illustration showing the concept of Spectral Spread over a pixel column with 1080 micromirrors. The projected spectrum recorded over one pixel column consists of a few nanometers of light, which corresponds to the spectral spread of that particular pixel column.

To determine the spectral spread, spectrometer measurements with bitmap images shown in figure 2.4 were carried out. Since the light reflected of a single pixel column on the DMD is indiscernible to distinguish the signal from electronic noise generated by the spectrometer, a few columns of pixels were turned on and their spectrum was recorded. The change here from the spectral width measurements discussed earlier was that the experiments were performed such that the width of the ON pixel columns were gradually increased in steps of 10 pixels keeping the central pixel column constant. The increase in the number of pixels were equally distributed on either side of the central pixel column. This sequence is done for pixel columns 21, 31 and so on across the three regions of the spectrum.

For instance, referring to figure 2.11a, the central pixel column is 811. In the first reading, 21 pixel columns were turned ON, keeping the central pixel column fixed, i.e., pixel columns 801 to 821 were turned ON. The wavelength range of the spectrum obtained was 595 to 606 nm. Next the

number of pixel columns ON were increased to 31, i.e., pixel columns 796 to 826 were turned ON. The wavelength range of the spectrum obtained was 592 to 608 nm. Subsequently, the number of pixel columns ON were increased to 41, 51 and 61 i.e., pixel columns 791 to 831, 786 to 836, 781 to 841 were turned ON respectively. The wavelength range of the spectrum corresponding to these were 591 to 610 nm, 589 to 612 nm and 588 to 615 nm respectively.

In order to obtain the spectral spread for a single pixel column, reverse extrapolation was done from the measurements conducted above. By calculating the average from the readings, an approximate measure of the number of wavelength intervals that influence a single pixel column across the three regions of the spectrum was determined. The plots obtained by reverse extrapolation for two readings across the VIS and IR region of the spectrum is shown in the figure 2.11.

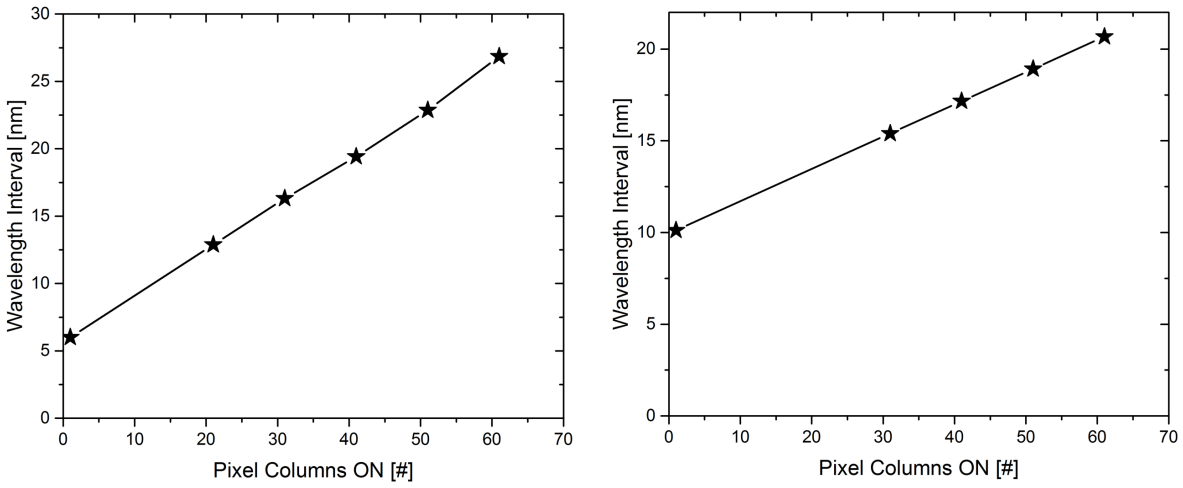

(a) Plot of Spectral Spread variation for a central pixel column 811 in the VIS region of the spectrum.

(b) Plot of Spectral Spread variation for a central pixel column 1121 in the IR region of the spectrum.

Figure 2.11: Plots showing the reverse extrapolation results of Spectral Spread data to determine the number of wavelengths influencing a single pixel column.

From the experiments it was determined that the spectral spread in the UV region was approximately 3 nm/px, which is to say an influence of 3 nm of wavelength interval on a single pixel column in the UV region can be expected. For the VIS and IR region, the spectral spread was determined to be 6 nm/px and 10 nm/px respectively. It should be noted that the spectral spread in the IR region and UV region are not very accurate due to the limitations of the Avantes spectrometer in providing a strong signal to noise ratio in these regions and hence an rough estimate was made using limited measurements. Further investigation might be needed to confirm the estimates in the UV and the IR region.

2.3.3. Intensity Variation on the DMD

This section details the current measurements done to determine the intensity variation along a column of micromirrors (1080 micromirrors in the Y-direction) of the DMD. Spectrometer based measurements could not be employed here, as the number of micromirrors to be turned ON needs to be reasonably high - greater than 5000 micromirrors (5 complete pixel columns) as seen in section 2.3 for a measurable signal on the spectrometer. The intensity variation trend along a column of pixels cannot be identified with this large number of pixels and thus current based measurements were used for this section.

As mentioned earlier, a high resolution ammeter in the nano-Ampere range was used for measurements in this section. As the current output from a single pixel was lower than 1 nA, they could not be recorded due to practical limitations. Thus a novel scan pattern was employed to control the

light projected on the DMD in this section. A bitmap image of dimensions 1080×1920 pixels with a black background, a small square shaped block of size 50×50 pixels kept white was developed using MATLAB. By loading this image on the DMD, the mirrors corresponding to this square white block will be turned ON. This square white block will be addressed as "SUPERPIXEL" from here on. By shifting this superpixel along a column of mirrors the intensity variation can be determined. A sample sequence of superpixel scan pattern is shown in figure 2.12.

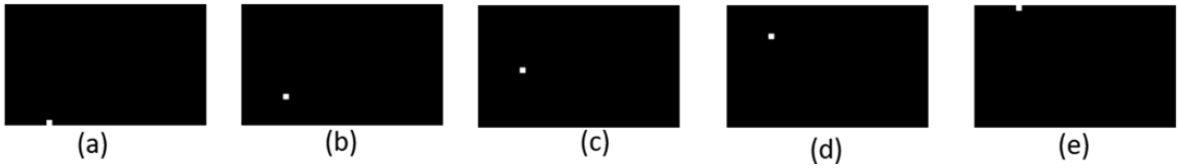

Figure 2.12: The figure represents the superpixel position for fixed pixel columns (401-450 in the X-direction). The superpixel position in the pixel row range (Y-direction) are - 1-50, 251-300, 551-600, 801-850 and 1031-1080 in the figures (a),(b),(c),(d),(e) respectively.

Due to time limitations, sweeping the superpixel across all the rows and columns of the DMD was not possible. Hence five intervals namely - 1-50 pixels, 251-300 pixels, 551-600 pixels, 801-850 pixels, 1031-1080 pixels along the Y-axis of the DMD for a fixed set X-axis coordinate was chosen. By moving the superpixel to these intervals along each set of column of mirrors, the current variation which is a measure of the intensity variation trend can be quite reasonably determined.

The intensity variation plots for three such pixel column ranges - 401-450 pixels, 1126-1175 pixels and 1451-1500 pixels are shown in figures 2.13, 2.14a and 2.14b respectively.

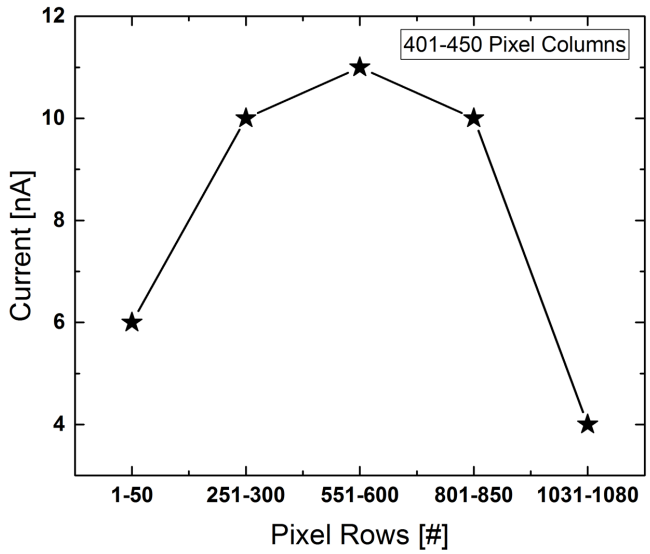

Figure 2.13: Intensity Variation along the width (Y-axis) of the DMD using Superpixel scan pattern for the pixel column range 401-450.

It can be seen that the intensity peaks at the centre of the DMD and follows an approximate bell curve shape. The intensity values are minimal at the edges of the DMD and this trend is true for all the pixel column ranges in the three regions of the spectrum. The pixel rows ranging from 251-850 (along the Y-axis) contribute to a significantly higher portion of the intensity than the other pixels on the DMD. This intensity trend will help in developing bitmap images for modulation schemes having ON pixels at the centre of the DMD. For instance modulation schemes based on Hadamard Transforms (details of which is discussed in section B) have the ON pixels mostly around the cen-

tral pixel range of 300-700 pixels. The intensity variation trend will be vital for such modulation schemes.

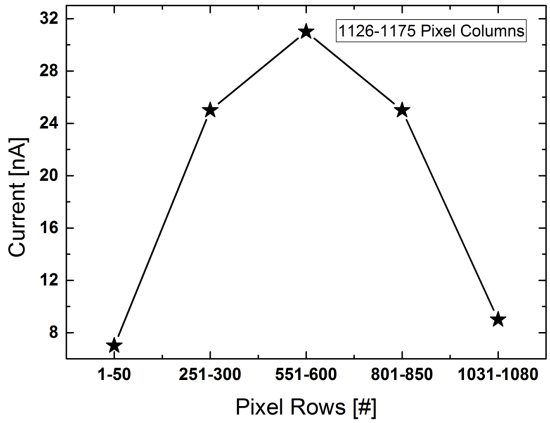

(a) Intensity Variation for the pixel column range 1126-1175 on the DMD.

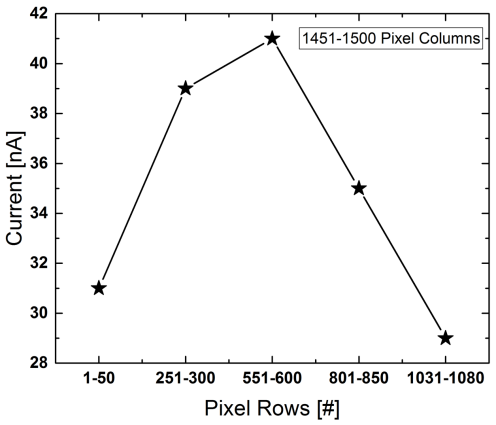

(b) Intensity Variation for the pixel column range 1451-1500 on the DMD.

Figure 2.14: Intensity Variation along a column of micromirrors (Y-axis) of the DMD using superpixel scan pattern. The intensity is highest at the centre of the DMD and the intensity variation trend approximately follows a bell curve.

Furthermore in the same measurements, the wavelength curvature based assumption was also validated. To recap it was assumed that a wavelength interval aligns perfectly along a column of micromirrors (1080 micromirrors in the Y-direction). For example when a wavelength interval say 495-500 nm is projected on the DMD, it is assumed that they lie along the same pixel column range from the bottom of the DMD to the top of the DMD.

To validate this, a 20 nm band-pass filter was used to determine the wavelength curvature along the Y-axis of the DMD. For this, the same superpixel based current measurements were used, but this also required that the superpixel be scanned along the X-axis of the DMD to cover the spread of the wavelength interval on the DMD (in the X-axis) when 20 nm of light is projected. The results of these measurements are plotted in figures 2.15, 2.18 and 2.17.

The figure 2.15 is a result of using a 640 nm band pass filter such that only wavelengths from 631-650 nm are projected on the DMD. During these experiments the superpixel was first scanned along the Y-axis (1080 pixels) in the intervals of 1-50, 251-300, 551-600, 801-850 and 1031-1080 pixel rows. That is 5 readings along the Y-axis for a fixed pixel column range on the X-axis, for example- 825-875 pixel columns. Next the superpixel was shifted by 25 pixels along the X-axis, i.e., to the pixel column range 850-900 and the same scan pattern (5 readings) is followed for the Y-axis as explained earlier. This sequence is followed along the X-axis scan until the current is almost zero, (example beyond the 950th pixel column in this case). The same holds true for the readings preceding the 800th pixel column. The overlap of 25 pixels in the above case is continued for the complete scan pattern for the following reason - the actual current values obtained when the superpixel is in the column range 825-875 will be averaged out to be at pixel column number 850 for ease of calculation. The next superpixel block will then be moved to column range 875-925 in a general scan pattern and the current value will be averaged out to pixel column number 900. But in the case discussed above, with a 25 pixel overlap, the superpixel will be moved to the pixel column range 850-900, the current value can be averaged out to be at the pixel column number 875 and this will give a better resolution of the wavelength curvature distortion (i.e, will provide more data points for the curve). Thus this method is adopted and the shift and overlap of 25 pixels for each scan along the X-axis of the DMD is carried out. By using this scan pattern, the current values obtained which correspond to the intensity of light is plotted in figure 2.15.

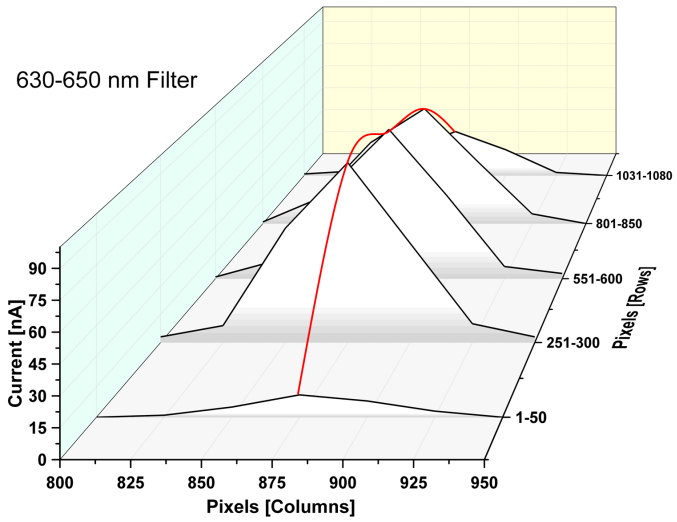

Figure 2.15: The wavelength curvature when using a 640 nm filter with a 20 nm band-pass. The projected wavelength is thus in the wavelength interval 631 to 650 nm. The wavelength curvature in this interval is unbending and along the column of pixels in the Y-direction of the DMD.

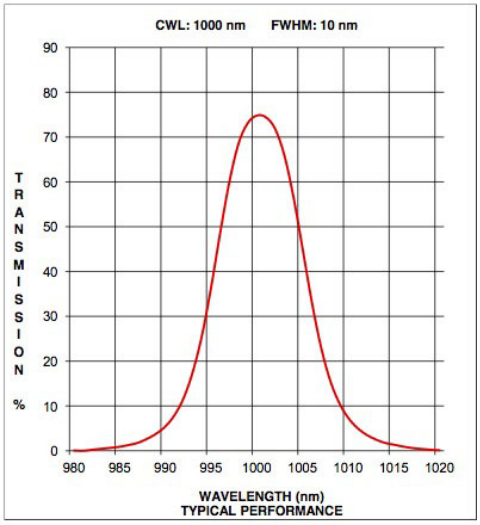

Figure 2.16: Sample transmission curve for a 10 nm band pass filter having a central wavelength of 1000 nm. The peak transmission is generally close to the central wavelength of the particular band pass filter [36].

From the figure 2.15 it can be seen that, the wavelength spread along the X-axis is across 150 micromirrors. It can be seen that this spread is close to a bell curve shape with the current values peaking at the centre of the pixel column range for the particular band-pass filter and then tapering off on either sides. This trend can be attributed to the transmission curve of a typical band pass filter shown in figure 2.16. The transmission is usually highest close to the central wavelength and decreases on either sides of it resembling a bell curve. The use of a 20 nm band pass filter in the experiments, thus have the highest intensities close to the central wavelength of each filter and tapers off on either sides of it. Further this trend is also seen for all the five intervals in the Y-axis along the 1080 micromirrors of the DMD. The intensity is higher at the centre of the DMD (pixel row range 251-850) as seen in the earlier intensity variation experiments and they follow a bell curve shape both along the X-axis and the Y-axis. By combining the two trends, along the X-axis and Y-axis, an

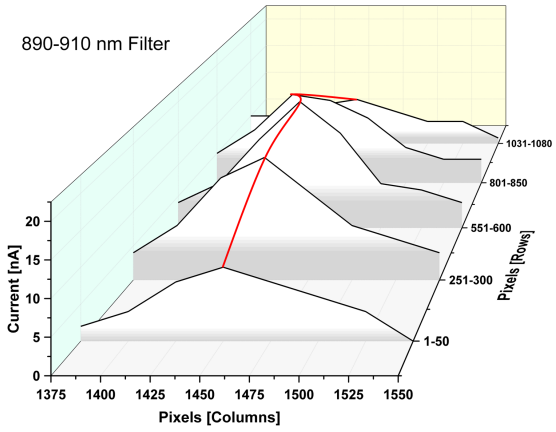

Figure 2.17: The wavelength curvature when using a 900 nm filter with a 20 nm band-pass. The wavelength curvature in this interval is distorted with the peak intensity shifting to the left of the assumed pixel column range by 25 pixel for the pixel row range 650 to 900.

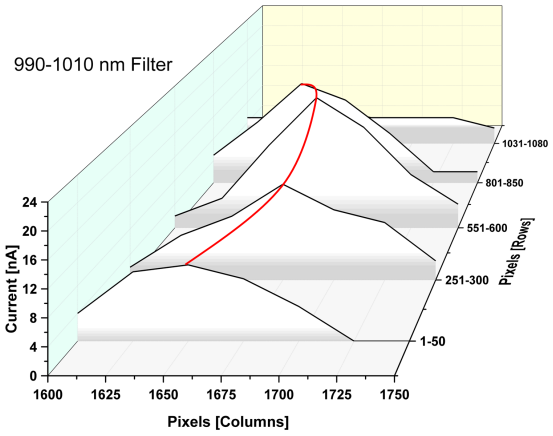

Figure 2.18: The wavelength curvature (red curve) when using a 1000 nm filter with a 20 nm band-pass. The wavelength curvature in this interval is bent with the central higher intensity part shifted right by 25 pixels from the lower intensity along the edges.

approximate wavelength curvature for this wavelength interval can be approximately determined. The average shape of the wavelength interval is assumed to be along the highest points of the curves along both the X-axis and Y-axis. This concept is clearer with the figure 2.15. The red curve traversing the peaks along both the X-axis and Y-axis of the DMD is a close estimate of the wavelength curvature for the wavelength interval 630 to 650 nm.

The experiments revealed that the wavelength curvature for all the wavelength intervals was unbent and straight along a column of pixels for the UV and VIS region of the spectrum. Though the wavelength curvature for most of the wavelength intervals in the IR region were unbent, there existed an anomaly for two wavelength intervals corresponding to the 900 nm and 1000 nm band pass filter. In these two cases the wavelength curvature was distorted as can be seen in figures 2.17 and 2.18. The exact reason for this anomaly could not be confirmed as the shift is not uniform for the pixel column or pixel row ranges in the IR region of the spectrum. A possible reason could be the error in measurement as the current values are very close to one another for a clear difference. If this is taken into account, probably the wavelength curvature of the wavelength interval 890 to 910 nm might be along a straight line as well.

Another possible reason can be attributed to the presence of artifacts in the optical system. Artifacts are errors introduced in scientific investigations due to preparative or investigative procedures. Optical elements like lenses, mirrors, prisms are generally fabricated by grinding, smoothing and polishing. A common issue with these fabrication processes are the artifacts, which can be localized at different points on the optical surface. These artifacts affect the imaging performance of optical systems, but the influence and extent of these artifacts have not been fully analyzed yet [37]. In the FOMS optical system, the artifacts could be introduced due to the various mirrors and lenses used.

2.4. Conclusions

In this chapter the optical system of the FOMS prototype was investigated and characterized. It was determined that as much as 99% of the light in the UV, IR region and 96% of light in the VIS region of the spectrum was lost while traversing through the optical path before reaching the solar cell at the exit of the setup. The existing optical path was missing a part of the spectrum in the UV region

and for this the optical path was optimized to projected the complete spectrum onto the DMD. The different assumptions made by the DST team were validated and the conclusions relating to the assumptions discussed in the beginning of the Chapter 2 are as follows:

- Conclusion 1 - Spectrometer measurements using line scan pattern proved that the spectral width varied across the different regions of the spectrum. It was 2.11 px/nm, 2.24 px/nm and 2.32 px/nm for UV, VIS and IR regions respectively. One possible reason for this trend could be the shift in the optical plane of the DMD with respect to the optical plane of the flat field diffraction grating. This causes the light in the VIS and IR region to travel an extra distance to be projected on the DMD when compared to the light in the UV region, thus having a wider spectral width.

- Conclusion 2 - The spectral spread, which is a measure of the number of wavelength intervals influencing a single pixel column was determined using the line scan pattern and the spectrometer. It was determined that the spectral spread varied across the three regions of the spectrum - UV, VIS and IR as 3 nm/px, 6 nm/px and 10 nm/px respectively.

- Conclusion 3 - Current based measurements using superpixel based scan pattern showed that the intensity was highest at the centre of the DMD, in the pixel row range (Y-axis) 251-850 and the intensity was much lower along both the edges of the DMD. Further the intensity variation along a column of micromirrors was close to a bell curve shape for all the 1920 pixel columns on the DMD.

- Conclusion 4 - Current based measurements with a 20nm band-pass filter using the superpixel based scan pattern revealed that all the pixels in a pixel column have the same central wavelength in the UV and VIS regions of the spectrum. This was true for some wavelength intervals in the IR region as well. But for the wavelength intervals 890 to 910 nm (figure 2.17) and 990 to 1010 nm, the wavelength curvature was distorted (figure 2.18). The reason for this could be attributed to the presence of artifacts in the FOMS optical system.

3

Development of FOMS Model

The goal of this chapter is to explain the development of a model which simulates the working of the FOMS prototype developed by the DST team. The model was developed to predict the spectrum on every pixel of the DMD and a resultant current output from a solar cell illuminated by light reflected off the DMD, when an image is loaded on the DMD. Further the different building blocks (sub-functions) developed to build the model have also been detailed. The model has been developed to accommodate different post processing steps corresponding to different modulation schemes that can be developed in future. The post processing steps can be incorporated as add-on sub functions to the main function without changing the core of the model.

3.1. Need for the model

The FOMS prototype developed by the DST team has a modulation scheme that is inspired by Michelsons interferometer. The bitmap images generated as a result of this scheme follows a sinusoidal pattern mimicking the motion of the moving mirror in the Michelsons interferometer as mentioned in the section 1.4.2. In operation of the FOMS prototype the complete set of bitmap images are loaded onto the DMD and each image is displayed on the DMD chip for a prescribed display time. The DMD mirrors are either switched ON or OFF based on the image displayed at any given instant and the light deflected off the DMD is incident on the solar cell (both the calibrated cell and device under test). The solar cell produces a current for each image loaded on the DMD and this is recorded. The current values corresponding to all the images are then fed to the electrical circuit. The electrical circuit consists of a transimpedence current pre-amplifier that amplifies and converts the current signal to its voltage equivalent. The voltage values are then digitized by means of an analog-to-digital converter (ADC). It should be noted that each image gives rise to a corresponding current value and thus an ADC count. These ADC values are then post-processed to get the EQE of the solar cell. The post-processing step currently in place is based on inverse Fourier transforms. The biggest limitation of the current prototype is that it is not flexible to test any new modulation schemes. The images based on new modulation schemes which can be generated using MATLAB scripts can be mounted on the DMD, but the post-processing step which needs to be altered suitably cannot be integrated in the existing setup. Thus the ADC counts obtained as output have no much meaning. It is only when the ADC counts are post-processed that we obtain useful information thus limiting the flexibility of the FOMS prototype.

Recent advances in digital image processing technology have shown that alternate schemes like Hadamard transforms and Wavelet transforms are more suitable for image processing due to their mathematical simplicity and energy compaction capabilities [38]. This would make them more suitable for the FOMS setup but using these modulation schemes and their corresponding transforms is not possible using the current prototype. In order to overcome this limitation, a model that

mimics the working of the existing setup is developed. The model will be able to generate current output corresponding to images developed from different modulation schemes. This development of a model is thus vital to test and validate different modulation schemes with their corresponding post-processing steps which can be developed as independent add-on sub-functions. The results of the experiments based on the characterization of the FOMS optical system discussed in chapter 2, will form the base for the model development.

The model needs to be developed such that it can predict the spectrum incident on every pixel of the DMD. This also translates to the spectrum on every pixel of a bitmap image loaded on the DMD, due to the 1-to-1 correspondence between the DMD and the image. The 1-to-1 correspondence arises out of the pixels on the images (1920×1080) and micromirrors on the DMD (1920×1080). For this the following assumption was made, the spectrum incident on every pixel of the DMD is assumed to be Gaussian and is characterized by 3 parameters - the central wavelength corresponding to each pixel column, the spectral spread over a single pixel column and intensity distribution over each pixel. The following sections detail the different sub-functions that were developed in order to realize a model that was described earlier.

3.2. Pixel Column to Central Wavelength Mapping

This step follows from the discussion on spectral distribution on the DMD from section 2.3. From the spectral width measurements discussed in section 2.3.1, it was known that one nanometer of light is projected over a few pixels columns which varies across the three regions of the spectrum. Also the spectral spread measurements discussed in section 2.3.2, showed an influence of more than 1 wavelength interval over a single pixel column. The information from these two measurements were used to create a mapping function, which would enable mapping every pixel column approximately to its central wavelength.

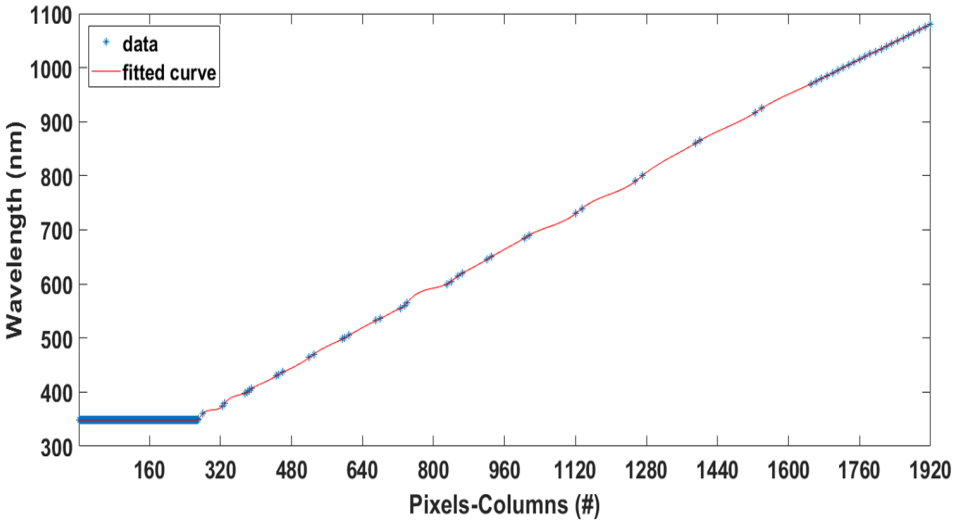

Figure 3.1: A curve fit used to map the 1920 pixel columns on the DMD to their corresponding central wavelengths of the spectrum. The scattered data points between the pixel columns 270 and 1650 are actual measurement data points and the rest are assumed data points based on Spectral width measurements.

The technical limitations of the spectrometer meant that measurements were possible between the wavelengths 350 nm and 1005 nm. In the IR region beyond the 1005 nm and up to 1050 nm, excess electronic noise in the spectrometer readings meant that the central wavelengths and their corresponding pixel columns could not be estimated. Thus the pixel columns of all the wavelengths

beyond 1005 nm were estimated based on the spectral width calculation in section 2.3.1. Further the experiments suggested that the pixel column 270 roughly corresponds to wavelength 350 nm. All the pixel columns preceding 270, were assumed to have a central wavelength corresponding to 349 nm for the purpose of fitting a curve accurately.

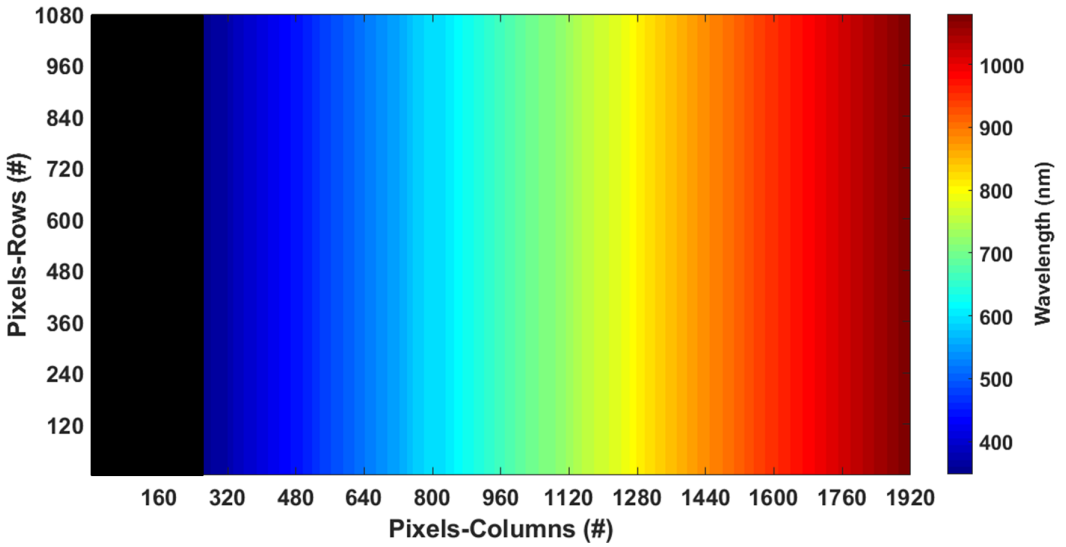

Figure 3.2: Distribution of the projected spectrum across the 1920 pixel columns on the DMD. Light of wavelength 350 nm falls on the pixel column number 270, preceding which there is no light incident. For illustration purpose this region is darkened.

The distinctive pairs of pixel columns and central wavelengths were then fitted with a 'Smoothing Spline' fit (shown in figure 3.1) to map all the pixel columns to their respective wavelengths. The mapping was developed on MATLAB. The spectrum of interest ranges from 350 nm to 1050 nm. But there exists enough pixel columns to accommodate even wider spectra on the DMD. This mapping information was then used to create a matrix of dimensions 1080×1920 (resembling the dimensions of the DMD) to represent the spectral distribution of the wavelengths of the projected spectrum across the DMD which is show in figure 3.2. The pixel columns corresponding to the three regions of the spectrum as a result of this mapping are as follows - UV region extends from pixel column 270 to 379, the VIS region extends from pixel column 380 to 1040 and the IR region lies beyond pixel column 1040 up until 1920.

3.3. Correction Matrix

A correction matrix was developed using current measurements that were performed in chapter 2 to describe the intensity variation in the Y-direction (across the 1080 pixels) of the DMD. The idea is to use this matrix as a multiplying factor with either the intensity or photon flux variation over the DMD to get an accurate reading of the same. A MATLAB script was written to generate this matrix.

The current values (which is a measure of intensity of light) over a column of mirrors determined in the superpixel based current measurements (described in section 2.3.3) were the input parameters. The current measurements were determined at five different row intervals along the width of the DMD (1080 mirrors), i.e., in the pixel range – 1-50; 251-300; 551-600; 801-850 and 1031-1080 pixels. To develop the matrix the centre of the pixel row ranges were considered to be the points of measurement – i.e. – readings at pixels 25, 275, 575, 825 and 1055 were assumed to be the measurement data points. Since the number of pixels in a superpixel that was defined earlier is 2500 (50 pixels×50 pixels), the current values obtained were divided by 2500 to get the approximate current

value corresponding to a single pixel at the pixel positions 25, 275, 575, 825 and 1055. Note all the above pixel positions are pixel row values in a single pixel column. Next, the intermediate current values (between pixels 26 to 1054) were determined using 'Spline' interpolation using the above data. The current measurements across the edges of the DMD – pixels 1-24 and pixels 1056-1080 were then found using extrapolation from the data across the pixels 25 to 1055 done before. This procedure gave the current values across all the micromirrors/pixels in a single pixel column on the DMD. This data was then normalized to get the actual multiplying factors.

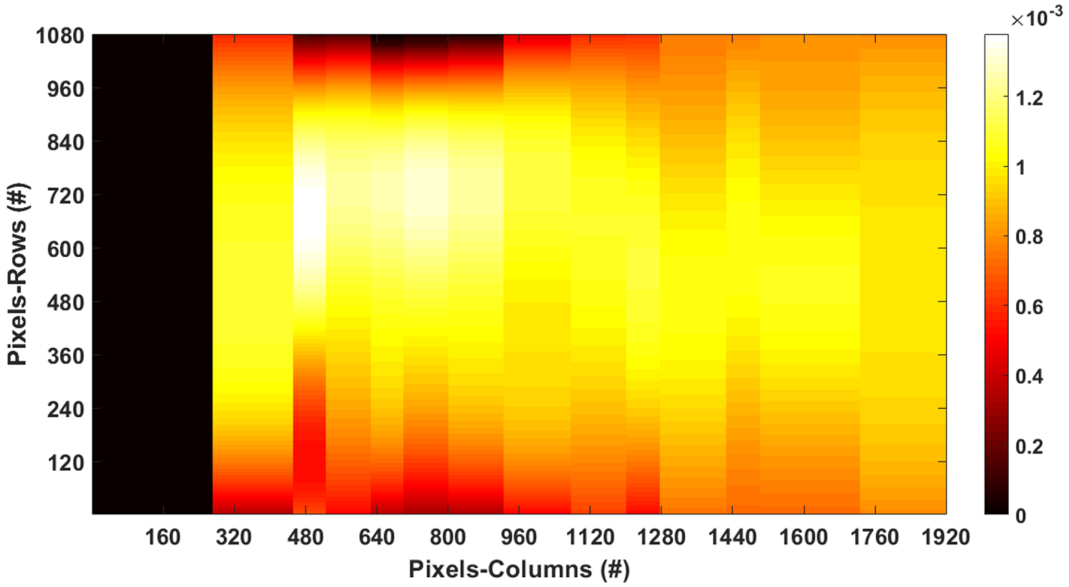

Figure 3.3: Correction Matrix with intensity multiplying factors across the DMD. Preceding pixel column 270, there is no light projected on the DMD, hence the multiplying factor for pixel columns 1 - 269 is 0.

The above step is then repeated for all the superpixel scans along the length of the DMD (1920 columns), which provided with the normalized intensity variation on the DMD. This data was then used to create a correction matrix of dimensions 1080×1920, see figure 3.3, which has the multiplying correction factor for the intensity variation data for all the columns and rows of the DMD.

3.4. Intensity & Photon Flux Variation Matrix

The next sub-function developed was the Intensity Variation matrix over all the 1920 pixels columns (X-axis) of the DMD. To develop this, the following data was used

- Information based on the previous two sub-functions - Pixel column to Central wavelength mapping (figure 3.2), Correction Matrix (figure 3.3).
- Spectral information when a white image is mounted on the DMD (all mirrors of the DMD turned ON).
- Results based on the spectral measurements discussed in section 2.3.1

An empty matrix of dimensions 1080×1920 was created first which will have the intensity values corresponding to different pixel columns. All the 1920 pixel columns of the DMD was mapped to their corresponding central wavelengths as described in section 3.2. Next the intensity corresponding to these wavelengths are determined as follows. The wavelengths and corresponding intensity values of a white image mounted on the DMD is shown in figure 2.2. From this data, the photon flux for the different wavelengths of the spectrum was calculated using equation 3.3. Combining this

information with the pixel column to central wavelength mapping, the photon flux and intensity values corresponding to all the pixel columns of the DMD was determined. This data was saved as a ***mat*** file which can be loaded as a sub-function on MATLAB.

The energy (in joules and eV) per incident wavelength was calculated using equations 3.1, 3.2

$$E(J) = \frac{hc}{\lambda(m)} \tag{3.1}$$

where,
h - Planck's constant ($6.625 \times 10^{-34} m^2 kg/s$)
c - speed of light ($3 \times 10^8 m^2/s$)

$$E(eV) = \frac{1240}{\lambda(nm)} \tag{3.2}$$

The spectral photon flux was then calculated using equation 3.3

$$\phi = \frac{1.24 \times I}{q \times E} \tag{3.3}$$

where,
ϕ - Spectral Photon Flux ($m^{-2} s^{-1} nm^{-1}$)
I - Incident spectral Irradiance ($W m^{-2} \mu m^{-1}$)
q - electron charge (1.6×10^{-19} C)
E - Energy (eV)

Finally, as described in section 2.3.1, each nm of light has a specific spectral width across the three regions of the spectrum. To recapitulate, the spectral width is 2.11 px/nm; 2.24 px/nm and 2.32 px/nm across the UV, VIS and IR regions of the spectrum respectively. Thus the final step was to divide the intensity and photon flux corresponding to all the pixel columns that was determined in the previous step, to their corresponding spectral width's to get the actual intensity and photon flux at each of the 1920 pixel columns. This process was then repeated over all the pixel columns of the DMD and the values was used to fill the empty matrix created in the beginning with Spectral Intensity and Spectral Photon Flux values. The variation of the Spectral Intensity and Spectral Photon Flux across all the pixel columns of the DMD is shown in the figures 3.4 and 3.5 respectively.

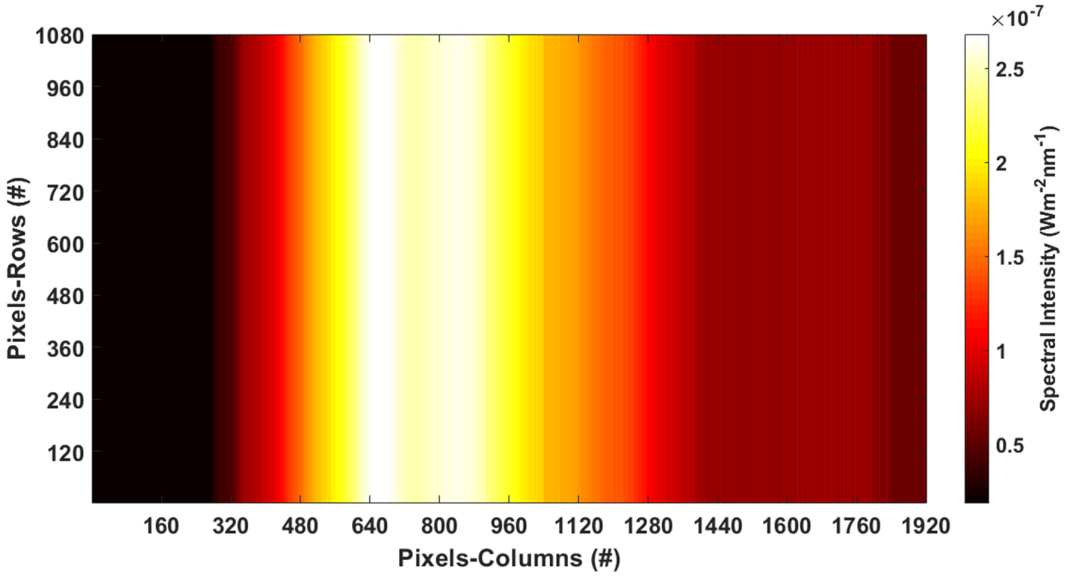

Figure 3.4: Spectral Intensity Variation over the DMD. The highest intensity is in the pixel column range 500 to 1000 which corresponds to the VIS region of the spectrum. The intensity in the UV and IR regions of the spectrum are lower in accordance to the white image spectrum on the DMD (2.2).

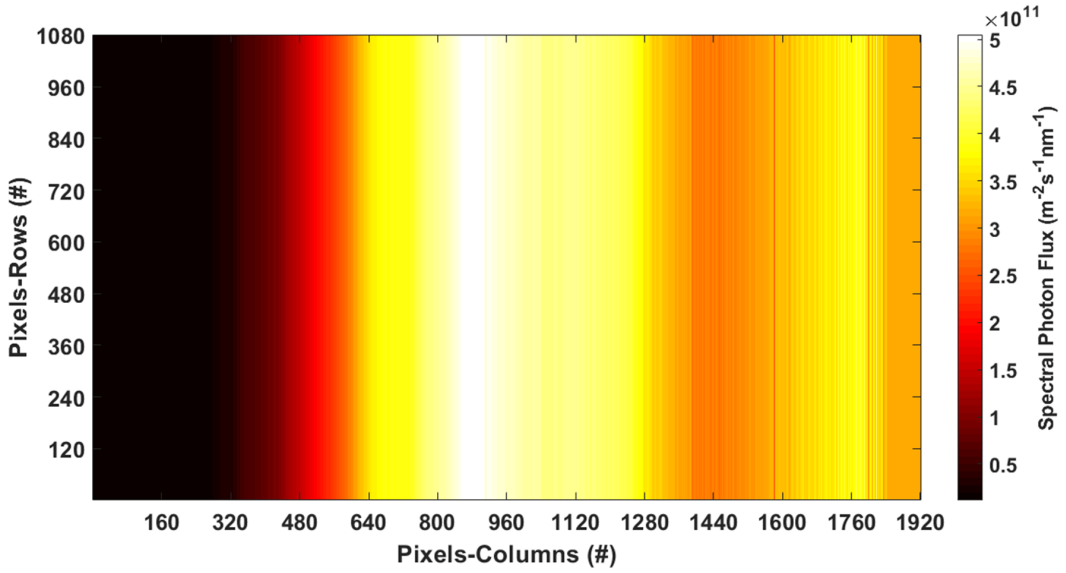

Figure 3.5: Spectral Photon Flux Variation over the DMD. The spectral photon flux for the 1920 pixel columns is calculated combining the pixel column to central wavelength mapping and intensity values obtained with a white image mounted on the DMD.

3.5. Spectral Spread Matrix

As described in the section 2.3.2, every pixel column on the DMD has an influence of more than one wavelengths on either side of its corresponding central wavelength. The number of wavelengths influencing a single pixel column varies across the spectrum and for the model purpose, an average of the spectral spread across the three regions of the spectrum is considered. It was determined that a pixel column in the UV region had an influence of around 3 nm of light, hence having a spectral spread of 3 nm/px. Likewise, the VIS and IR region of the spectrum also had spectral spreads of 6 and 10 nm/px. Figure 3.6, provides the spectral spread information over the entire DMD. The matrix

was developed using MATLAB. The actual model developed using the main function will take this into account while calculating the current generated from the solar cell when an image is loaded on the DMD.

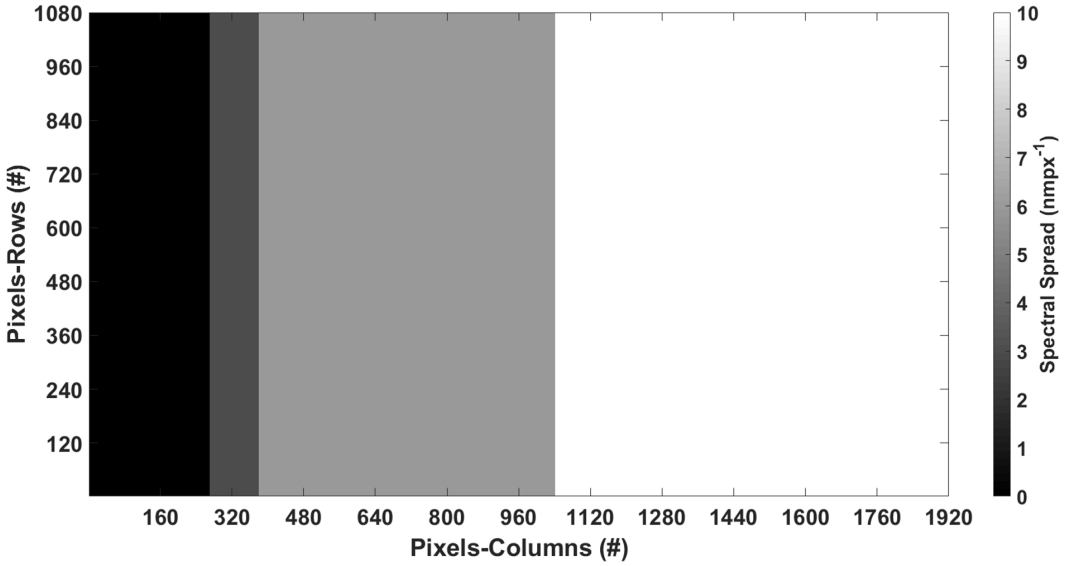

Figure 3.6: Average Spectral Spread over the DMD generated using a MATLAB script.

3.6. Final Spectrum Calculation

The development of this sub-function involved Mathematical concepts like Gaussian distributions and Error functions which were used to determine the spectrum corresponding to each pixel on the DMD. In doing so, every time a new image is loaded on the DMD, the spectrum corresponding to the white pixels on the image will be mapped to their corresponding pixels on the DMD, which is 1-to-1 mapping. Also, the sub-function will form the core of the model in which all the other sub-functions developed earlier will be used to calculate the spectrum corresponding to each pixel on the DMD. The math behind it and how this sub-function works is explained next.

The approach behind the calculation of the spectrum for each image is shown in figure 3.8. A 3D matrix was created on MATLAB with the X and Y axis corresponding to the pixel columns (1920 pixels) and pixel rows (1080 pixels) and the Z-axis corresponding to the wavelengths of interest. The Z-axis is to accommodate the concept of spectral spread (wavelength influences on a pixel) discussed in section 3.5. For instance, if a pixel is ON in the column corresponding to the VIS region, there will be an influence of 6 nm of light on this particular pixel, thus by placing the wavelengths on the Z-axis, the influence of all the 6 nm of light can be summed and the net photon flux for that one pixel can thus be determined. This concept is illustrated in figure 3.8 for one pixel of interest.

The central idea of the model is to simulate the spectrum on all the pixels of the DMD when the diffracted light from the grating is projected on it using all the matrices discussed above. The concept of error function was used to determine the probability that a measurement, under the influence of normal distribution with a known standard deviation is within a certain distance from the mean value. The error function is a sigmoid function widely used in statistical computations to integrate a Gaussian curve between small finite limits [39].

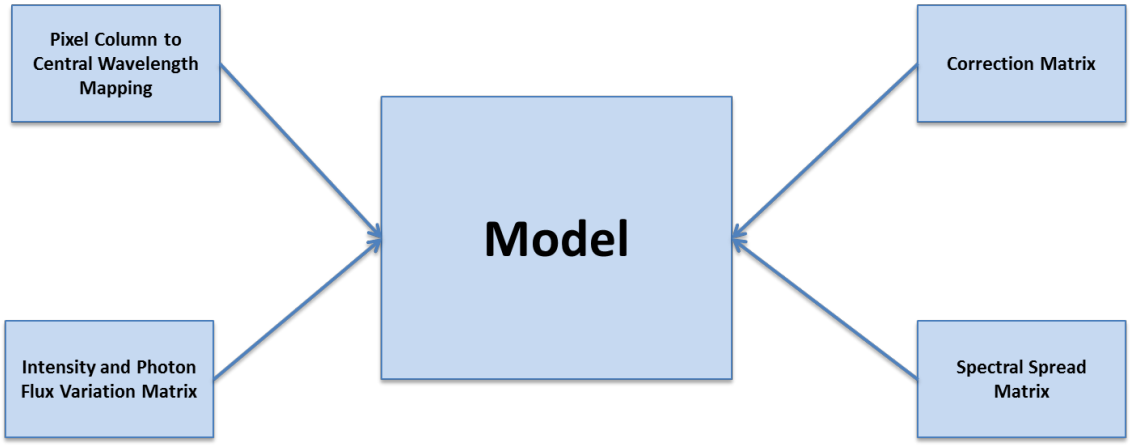

Figure 3.7: Schematic showing the different sub-functions designed to develop the model to mimic the working of the FOMS prototype.

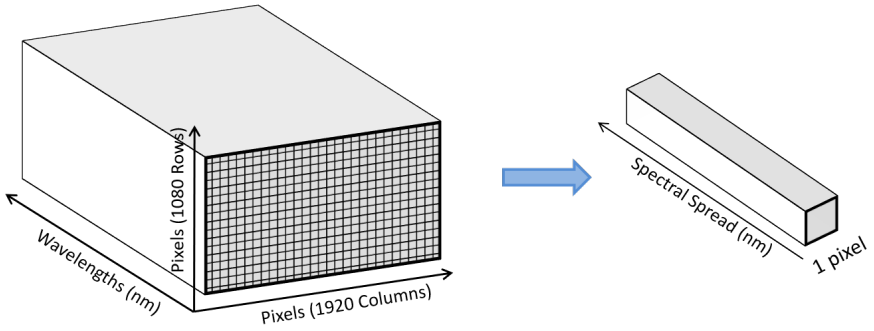

Figure 3.8: A schematic of the DMD Spectrum Model. The Z-axis corresponding to one pixel is to accommodate the spectral spread (wavelengths) of the pixel chosen. The spectral spread depends on the region where the pixel and pixel column exist on the DMD.

Figure 3.9 shows how an error function can be used to calculate the probability is a Gaussian random variable. If X is a Gaussian random variable with mean 0, standard deviation $\frac{1}{\sqrt{2}}$, the probability $P(-x \leq X \leq x)$ is equal to erf(x). Mathematically an error function is defined for a variable x as follows [40]:

$$erf(x) = \frac{2}{\sqrt{\pi}} \int_0^x e^{-t^2} dt \tag{3.4}$$

By restricting the the computation of erf(x) when $x \geq 0$, as shown in figure 3.10, the area for determining the probability is also restricted to the positive X direction. This enables the calculation of the error function using the spectral spread across the three regions as the standard deviation and the mean which corresponds to the central wavelength for each pixel column. By evaluating the error function of every pixel column on the DMD and then multiplying this with the corrections matrix and photon flux variation matrix developed above, we can obtain the spectrum corresponding to every pixel over the entire DMD.

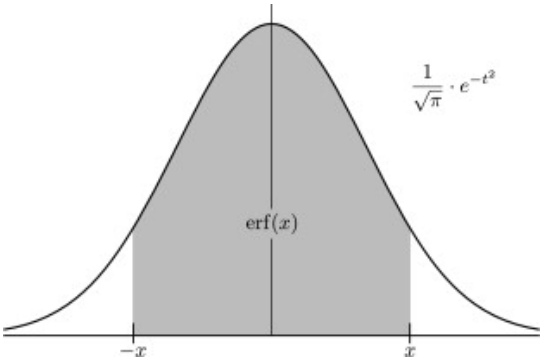

Figure 3.9: erf(x) is the probability that a certain Gaussian random variable lies in [-x,x] [40].

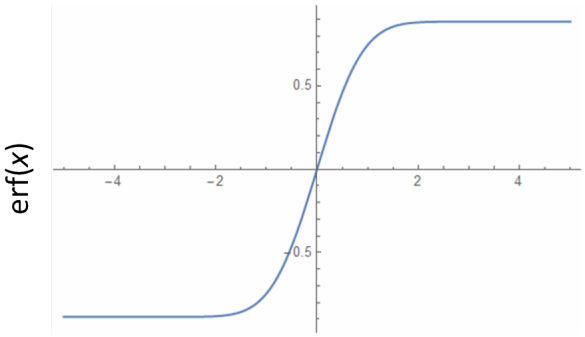

Figure 3.10: Plot of the error function [40].

The next step was to load all the images from a directory which correspond to a modulation scheme onto the 3D image matrix. The X and Y dimensions of this matrix correlate to the dimensions of each image (1920 pixels×1080 pixels). The Z dimensions of this matrix is determined by the number of images in the directory (user defined). Next the row number and column number of all the white pixels (ON pixels) on the image are determined using the FIND command. Subsequently all the white pixels that are found in an image is mapped to the respective pixels positions on the DMD due to the 1-to-1 congruence. This also provides the spectrum for each of the white pixels on the image and eventually the spectrum of all the white pixels for the image becomes the spectrum for that image. The final current for each image is then found by multiplying the spectrum with the EQE curve of the calibration cell and the electron charge (1.6×10^{-19} C). Repeating this process for all the images for a particular modulation scheme the overall current output for the calibration device is obtained. Repeating the same process under the same conditions with the device under test (DUT), a current output sans the EQE will be obtained.

The current generated should then be fed to a post-processing step in order to determine the EQE of the device under test. This post-processing step depends on the type of modulation scheme used to generate the images. For example when using a modulation scheme inspired by the Michelson interferometer, a post-processing step corresponding to Inverse Fourier Transform will be needed in order to get the final EQE of the DUT. Hence the post-processing step has not been realized in the current model as different modulation schemes have different post-processing steps and they need to be adapted congruously. But the model provides the flexibility to add suitable post-processing steps as add-on sub-functions for the calculation of the EQE.

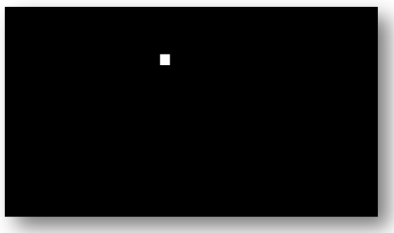

(a) Current output for the bitmap image with 3000 pixels ON was 0.179 μA. The ON pixels correspond to pixel columns 241 to 300 (60 pixels) and pixel rows 801 to 850 (50 pixels).

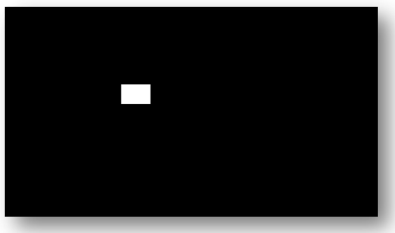

(b) Current output for the bitmap image with 15000 pixels ON was 0.8428 μA. The ON pixels correspond to pixel columns 401 to 500 (100 pixels) and pixel rows 601 to 750 (150 pixels).

Figure 3.11: Sample bitmap images used to test if the model was predicting a current output based on the sub-functions developed.

To test if the model was predicting the current output, different configurations of bitmap images were created and tested. Two sample bitmap images with their respective current outputs are shown in the figure 3.11.

Note - A brief introduction to a more suitable modulation scheme for image processing has been detailed in the Appendix B.

3.7. Conclusions

The goal of this chapter was to develop a model that simulates the working of the Fast Optical Measurement System. In this chapter the development of a model that could predict the spectrum on every pixel of the DMD was described. This was made possible by developing and integrating different sub-functions related to mapping of the pixel column with the central wavelength, intensity variation correction matrix, spectral spread based matrix and the intensity, photon flux variation matrix. Next, when an image is loaded on the DMD, the model determines the positions of the white pixels on the image and maps it to the matching pixels on the DMD. The spectrum corresponding to these white pixels and in turn the spectrum of every image is determined based on the sub-functions developed. Subsequently the model predicts the current output per image and the current output corresponding to all the images of a modulation scheme. Suitable post-processing steps can also be incorporated as add-on sub-functions to calculate the EQE of a device under test from the current output predicted by the model. The post-processing step has not been realized in the model as different modulation schemes will have different post-processing steps and they need to developed accordingly.

4

Model Validation

The aim of this chapter is to validate the model whose development was described in the last chapter. The validation is done using a monochromatic EQE based modulation scheme which was developed using MATLAB. For each image loaded on the DMD, the spectrum of incident light reflected by the DMD onto the solar cell changes. The spectrum reflected on to the solar cell depends on the ON pixels on the DMD which correspond to the white pixels in the image. Thus each image gives rise to a current value. A block diagram to illustrate this is shown in figure 4.1. The current output per image and total current output for all the images of the monochromatic EQE based modulation scheme, predicted by the model and the FOMS prototype is compared in this chapter.

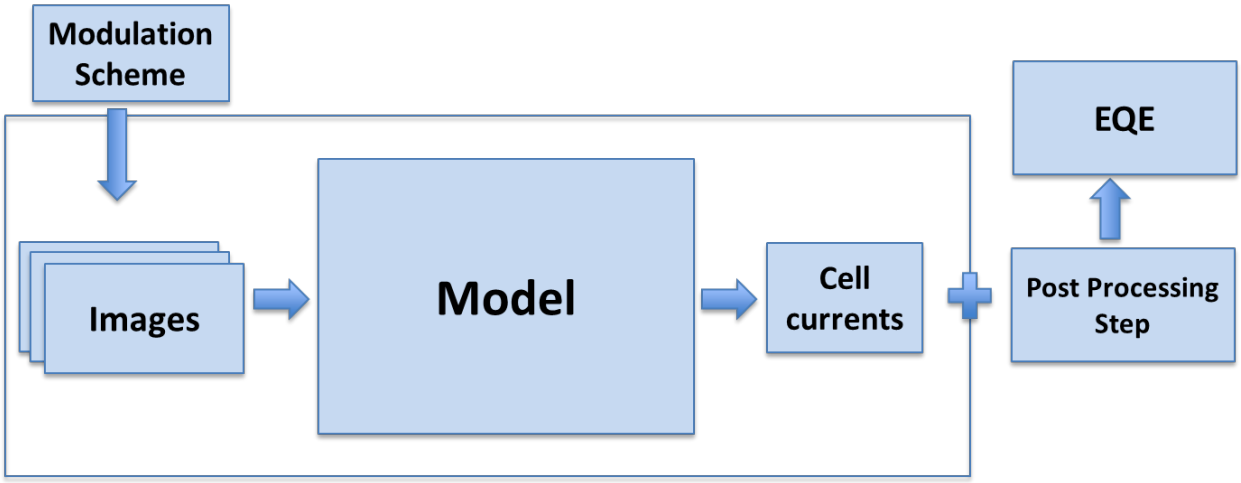

Figure 4.1: Schematic view of the block diagram of the model developed. The part enclosed within the inner rectangle has been realized. The modulation scheme and post-processing steps are interdependent and they need to be developed in relation to one another.

4.1. Validation of the Model

The preliminary step towards validation will be to use different image sequences and test the current output of the model and compare it with the current output of the prototype. The current post-processing step in the model is based on conventional EQE based measurements, i.e. calculation of current from incident photon flux (equation 4.1).

$$I_{SC}(\lambda) = EQE(\lambda) \times q \times \phi(\lambda) \tag{4.1}$$

where,
q - electron charge ($1.6 \times 10^{-19} C$)
$\phi(\lambda)$ - incident photon flux ($m^{-2} s^{-1}$)
$I_{SC}(\lambda)$ - short circuit current (A)

For the purpose of validation of the model, bitmap images (shown in figure 4.2) based on the monochromatic EQE based modulation scheme were developed. For this validation, the number of pixel columns ON were kept at five for each image. The line scan pattern used for this modulation scheme is shown in figure 4.2. The total number of images generated as a result of the monochromatic EQE based modulation scheme was 384 images (1920 pixels ÷ 5 pixels = 384). This means that the first image will have pixel columns 1-5 switched ON, the next image will have pixel columns 6-10 switched ON and so on. The final image (384th image) will have pixel columns 1916-1920 turned ON. This sequence thus ensures all the pixel columns on the DMD are turned ON in at least one image. Also, the whole incident spectrum will be reflected off the DMD onto the solar cell over the course of the 384 images. This set of images were then loaded on to the DMD and the output current for each image from the FOMS prototype was determined. The same images were then used to predict the current output from the model.

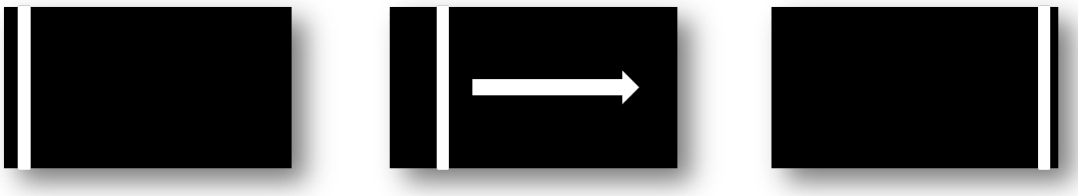

Figure 4.2: Bitmap images corresponding to a monochromatic EQE based modulation scheme. The number of pixel columns turned ON are fixed at 5 and this rectangular white block is scanned along the 1920 pixels as shown above (NOTE - the thickness of the white block in the above image is not 5 pixels, it is exaggerated to 100 pixels for illustration purpose).

The overall current output from the prototype was determined by connecting the calibrated solar cell to a high resolution ammeter (Keithley source meter 2400). But to determine the current output per image the output of the prototype which provides the current equivalent in ADC counts had to be calibrated and the following process was done for the same. Initially, the ADC counts when a black image was mounted on the DMD (all mirrors on the DMD turned to OFF position) was recorded. But the presence of electronic noise in the system meant that mounting the same black image again onto the DMD gave a different ADC count, i.e., mounting the same image on the DMD doesn't provide the same ADC counts for the two readings. In order to account for this error in measurement, the average of ADC counts obtained over 1000 readings of the black images was considered as the average ADC count for a black image and this was found to be 15330. The corresponding current output with the black image on the DMD from a calibrated cell was measured to be 1.73 μA. The same process was repeated for a white image (all mirrors on the DMD turned to ON position). The average ADC count for 1000 white images was 51620 and the corresponding current output from a calibrated cell was 73.56 μA. From this information an approximate ADC count for 1 μA of current was determined to be 505, using equation 4.2

$$ADC_{app} = \frac{ADC_{avg\_white} - ADC_{avg\_black}}{Curr_{white} - Curr_{black}} \tag{4.2}$$

where,
ADC_{app} - approximate ADC counts corresponding to 1 μA of current
ADC_{avg_white} - average ADC counts with white image on DMD
ADC_{avg_black} - average ADC counts with black image on DMD
$Curr_{white}$ - current output with white image on DMD
$Curr_{black}$ - current output with black image on DMD

Next the image sequence corresponding to the monochromatic EQE based modulation scheme (figure 4.2) were loaded on the DMD and the resultant ADC counts per image were recorded. It should be noted that to average out the ADC fluctuations due to electronic noise in the system, the sequence of images were loaded for 30 times under similar environmental conditions and the resultant ADC counts were averaged out for the 30 readings. The current output per image was then calculated based on equation 4.2. The final current output thus is the sum of all the current outputs from the 384 images. The same image sequence was then loaded onto the model and the current output for each image predicted by the model was recorded.

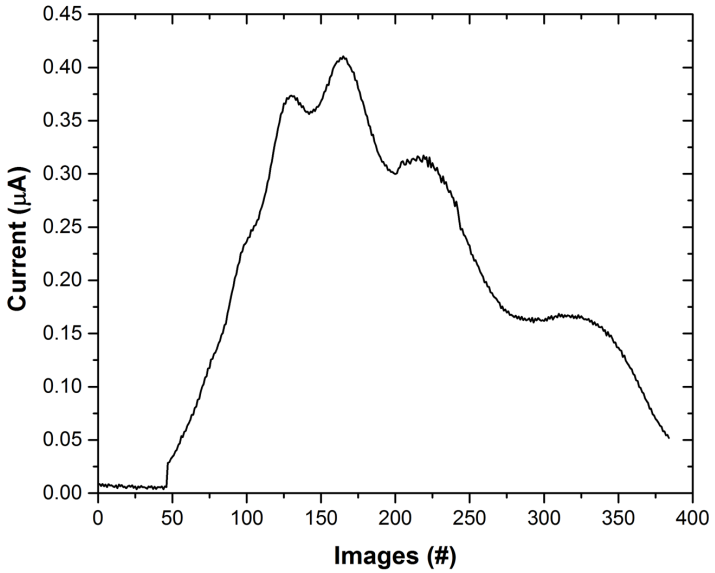

Figure 4.3: Measured current output per image for 384 images from the FOMS prototype. The modulation scheme is based on the monochromatic EQE scheme. The total current output from the prototype was 68.87 μA.

The figures 4.3 and 4.4 show a plot of the current output for each image, that was experimentally measured with the prototype and simulated by the model respectively. The overall current output had a deviation of 5.5 μA. Further the two plots also had current deviations per image which very significant in the image range 300-350. To verify if the simulated current by the model and the current generated by the prototype are off in other cases as well, the same monochromatic EQE based modulation scheme was used for another validation. This time the width of the rectangular region (figure 4.2) was increased to 10 pixels instead of 5 in the previous case.

The number of images as a result of this was 192 images (1920 pixels ÷ 10 pixels = 192). The first image will thus have pixel columns 1-10 switched ON, the next image will have pixel columns 11-20 switched ON and so on. The final image (192nd image) will have pixel columns 1911-1920 turned ON. The number of averagings were 30 in this case as well. The simulated current output

from model and the current generated by the prototype was then compared for the 192 images. The plots of these are shown in the figure 4.5.

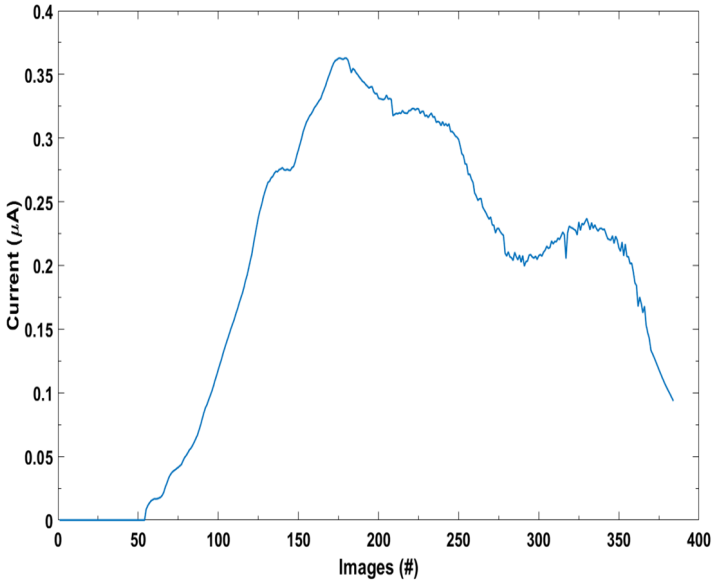

Figure 4.4: Simulated current output per image for the 384 images by the model for the same monochromatic EQE based modulation scheme. The total current output from the model was 74.37 μA.

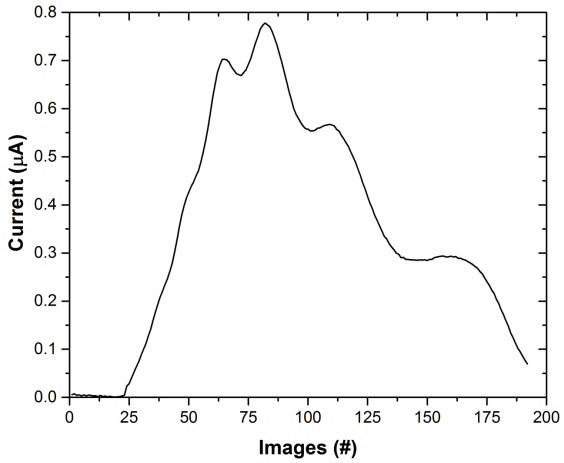

(a) Total measured current output for the 192 images from the prototype was 76.43 μA

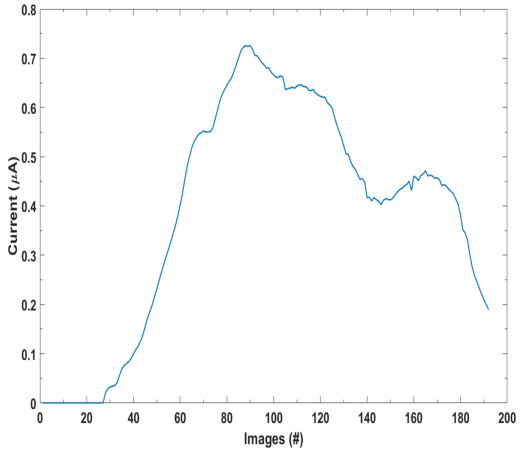

(b) Total simulated current output for the 192 images from the model remained 74.37 μA

Figure 4.5: Plot of measured current output of the prototype and the simulated current output from the model for 192 images based on monochromatic EQE based modulation scheme.

The current outputs from the prototype and the model were comparable with this new image sequence and the deviation was 2.06 μA. The error percentage was around 3% which is within the permissible limits. However there were still small variations in the current output per image between the two plots and this could be due to uncertainties in the prototype, aging and light bulb replacements that were done during the course of the measurements. Aging of the halogen light bulb affects the intensity of the incident spectrum, which directly influence the ADC counts of the system. The hardware limitations of the spectrometer meant that the intensity variation trend could

not be determined for individual pixels in a pixel column. The correction matrix developed to correct for this intensity variation (figure 3.3) for instance, has sharper blocks due to the limitations of the spectrometer and the model developed with a higher resolution spectrometer could possibly provide better output results.

Additionally, the measurements done for the characterization of the optical system which were used to develop the model, were done over a course of 4 months. The external lighting conditions, room temperature changes during the course of these measurements could also possibly have an effect on the ADC counts from the prototype. These reasons though cannot be conclusively said, could possibly be the reasons for variation in current output per image for images 150 and beyond.

Further, since the cumulative of all the white rectangular blocks in each image for all the 192 images will result in a complete white image, the total current output should be approximately equal to the current output with a white image on the DMD which is 73.56 μA. The current output of the model is approximately the same in this case, whereas the current output of the prototype is off by 2.87 μA.

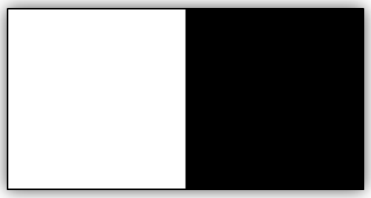

(a) Bitmap image with pixels 1 to 960 ON. The current output from the prototype with this image was 27.80 μA.

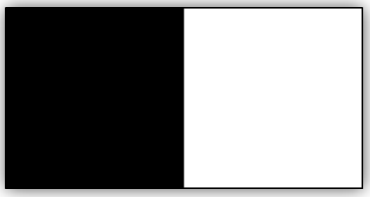

(b) Bitmap image with pixels 961 to 1920 ON. The current output from the prototype with this image was 44.472 μA

Figure 4.6: Bitmap images having a larger number of ON pixels to verify the ADC count based issue for validation of the model. Having larger number of ON pixels provides stabler ADC counts when compared to narrower rectangular block of ON pixels like in the monochromatic EQE based modulation scheme.

From the figures 4.3, 4.4 and 4.5 it can be seen that having a wider rectangular block or having larger number of ON pixels, the current output from the prototype is more comparable to the current output with a white image on the DMD. Thus to validate this, two bitmap images (shown in figure 4.6) were used to measure the current output from the model and the prototype. The number of averagings were 30 in this case as well. Since the two images when combined essentially form a white image, the sum of current outputs from the two images should be equal to the current output of a white image. On validating this, the simulated current output from the model remained at 74.37 μA and the current output of the prototype was 72.27 μA. Both these current outputs were in close approximation to that of the white image. Also, the difference in ADC counts between successive images were much smaller in this case, thus the ADC counts from the FOMS prototype were more stable in this case than the other two cases based on the monochromatic EQE scheme (figure 4.2) discussed earlier. Therefore, it can be hypothesized that in order to account for the prototype's repeatability in ADC count readings, having wider white region in the images might enable stabler ADC counts and thus a more comparable result.

4.2. Conclusions

The goal of this chapter was to validate the developed model by verifying if the current output per image and the total current output of the FOMS prototype and the model are comparable. Two modulation schemes based on monochromatic EQE system were developed to test the same. It was seen that though the total current output was comparable, the current output per image had some deviations. Possible reasons for changes in current output for each image could be due to

uncertainties in the prototype, aging of the halogen light bulb and light bulb replacements that were done during the course of the measurements. This could affect the intensity of the spectrum thus influencing the ADC counts. Hardware limitations during the characterization of the optical system meant that the input parameters (like intensity variation on the DMD) to the model had to be approximated which could also account for changes in the current output per image from the model. Further changes in room temperature and environmental conditions during the course of measurements could also affect the ADC counts.

Also for the prototype, having wider (10 or more) ON pixel columns provided stabler ADC counts and hence more comparable current output with the model when compared to narrower (around 5) ON pixel columns. The model also predicted the current output for different configurations of the monochromatic EQE based modulation scheme, thus proving that it can predict the current output for different image sequences based on other modulation schemes as well.

5

Conclusions and Recommendations

This chapter summarizes the important conclusions drawn from this thesis work and provides recommendations for future work that can be carried out with this as a foundation. The goal of this thesis work is restated from the introduction:

To investigate, characterize and model a promising fast EQE measurement technique called Fast Optical Measurement System developed by Delft Spectral Technologies team.

The above goal was divided into three sub-tasks mentioned below and the following sections will address the conclusions drawn from each of them.

1. Characterize the FOMS prototype by determining the optical losses, spectral distribution and intensity variation on the DMD.

2. Develop a model that simulates the working of the FOMS prototype by using the characterization results.

3. Validate the developed model by using a modulation scheme.

5.1. Conclusions

5.1.1. Characterization of the FOMS Optical System

The optical transmission losses between the entrance slit and the exit of the setup was around 99% in the UV, IR region of the spectrum and around 96% in the VIS region of the spectrum. Most of the light was lost in the interim - between the entrance slit and the solar cell at the exit of the setup. The main reasons for the same could be attributed to the poor efficiency of the flat field diffraction grating, overfilling of the DMD in the Y-direction in order to get enough light to be projected across all the 1080 micromirrors and the reflection, transmission losses of different optical components used in the setup. Other possible reasons for the optical losses could be surface reflection losses from the DMD micromirrors and losses due to DMD configuration - as the micromirrors on the DMD are not edge-to-edge connected.

Experiments also observed that a part of the spectrum in the UV region was not projected onto the DMD due to the position of the DMD with respect to the other optical components. The optical path was thus optimized by adjusting the heights and angles of different optical components like mirrors, mounting poles and lenses in the FOMS prototype. The current output after optimization increased by 18%, there by increasing the throughput of the setup.

Next the FOMS optical system was characterized using two measurements - spectrometer based measurements for determining the spectral distribution on the DMD and current based measurements for determining the intensity variation on the DMD.

A spectrometer was used for determining the spectral width and spectral spread of the projected spectrum along the X-direction (1920 pixels) and a high resolution ammeter was used for determining the intensity variation of the projected spectrum along the Y-direction of the DMD (1080 pixels). The characterization step also involved validating the assumptions made by the DST team while developing the prototype, the conclusions of which are presented below:

- The spectral width (the number of pixels columns occupied by a wavelength interval of 1 nm) was conducted with bitmap images using a line scan pattern. The spectral width in the three regions of the spectrum based on FWHM were - 2.11 pixels/nm in the UV region, 2.24 pixels/nm in the VIS region and 2.32 pixels/nm in the IR region. One possible reason for this trend could be the shift in the optical plane of the DMD with respect to the optical plane of the flat field diffraction grating (figure 2.9). This causes the light in the VIS and IR region to travel an extra distance to be projected on the DMD when compared to light in the UV region, thus having a wider spectral width.

- The spectral spread (the number of wavelengths intervals influencing the spectrum on a single pixel column) was determined using the bitmap images and a line scan pattern. The average spectral spread across the three regions of the spectrum were - 3 nm/pixel in the UV region, 6 nm/pixel in the VIS region and 10 nm/pixel in the IR region.

- The intensity distribution across the DMD (1080 pixels in the Y-direction) was conducted with bitmap images using a novel superpixel based scan pattern. The intensity variation was found to be close to a bell curve shape with the highest intensity at the centre of the DMD in the pixel row range 251-850. The intensities on either edges of the DMD tapered off to much lower values. This trend was true for all the 1920 pixel columns across the DMD.

- The anomalies with respect to wavelength curvature determination across the DMD (1080 pixels in the Y-direction) was conducted with a 20 nm band-pass filter using the superpixel based scan pattern. It was found that for all the wavelength intervals in the UV, VIS and for some wavelength intervals in the IR region all the pixels in a pixel column has the same central wavelength (lying in a straight line). For the wavelength intervals 890 to 910 nm (figure 2.17) and 990 to 1010 nm (figure 2.18), the wavelength curvature was distorted. The possible reasons for this could be attributed to the presence of artifacts in the FOMS optical system.

5.1.2. Development of the FOMS model

The results from the characterizing step were used as input parameters to develop a model that simulates the working of the FOMS prototype. Different sub-functions like the pixel column to central wavelength mapping (figure 3.2), spectral spread matrix (figure 3.6), correction matrix due to intensity variation (figure 3.3), intensity and photon flux variation matrix (figures 3.4 and 3.5) were developed using MATLAB. With the aid of these sub-functions and error function the model could determine the spectrum on every pixel of the DMD. When an image is loaded on the DMD, the position of the white pixels on the image is mapped to the corresponding micromirrors on the DMD due to a 1-to-1 correspondence between the two and the model then determines the spectrum of all the white pixels on the image and from it the current corresponding to each image is determined.

When an image sequence is loaded on the DMD, the overall current output will be the sum of the currents of each image and this can further be post-processed to get the EQE measurements. The post-processing step has not been realized in the model as different modulation schemes will have different post-processing steps. Thus based on the modulation scheme used to generate the

image sequence suitable post-processing steps also needs to be developed. The model though has the provision of integrating suitable post-processing steps as add-on sub-functions.

5.1.3. Model Validation

The developed model was validated by developing two modulation schemes based on a monochromatic EQE system. The current output for each image and the total current output for all the images of the modulation scheme were compared between the prototype and the model. The total current output was found to be approximately equal while the current output for each image had small deviations. Few possible reasons that can be hypothesized for the changes in current output for each image are - uncertainties in the prototype, aging and replacements of the light bulb that were done during the course of the measurements which affect the intensity of the spectrum thus influencing the ADC counts. Technical limitations of the spectrometer meant that the intensity variation trend could not be determined for individual pixels in a pixel column. The correction matrix developed to correct for this intensity variation (figure 3.3) might have a smoother trend across the pixel columns with a higher resolution spectrometer which could possibly provide better results from the model. The model also predicted the current output for different configurations of the monochromatic EQE based modulation scheme, thus showing that it can predict the current output for different image sequences based on other modulation schemes as well.

Thus in this thesis we described the development of a model to simulate the working of a promising fast EQE measurement technique called Fast Optical Measurement System. The model works satisfactorily to calculate the spectrum on each pixel on the image and subsequently the current output corresponding to different images in a modulation scheme. The model therefore is expected to be a valuable tool to test different modulation schemes and thereby improve the accuracy and speed of the EQE measurements with the FOMS.

5.2. Recommendations

The wavelength curvature shift discussed in section 2.3.3 was not realized for the wavelength intervals - 890-910 nm and 990-1010 nm as the anomaly was present only for these two wavelength intervals in the whole spectrum. The curvature distortion is not very pronounced (agrees with the assumption made by the DST team for most part of the pixels in a pixel column in the Y-direction) and hence curvature correction matrix was not developed. But having a matrix for this curvature correction can further improve the model.

(a) Exaggerated illustration of an assumed wavelength curvature on the DMD.

(b) Exaggerated illustration of a distorted wavelength curvature on the DMD.

Figure 5.1: The assumed wavelength curvature is straight along a column of pixels shown in figure 5.1a. The developed model is in accordance with this assumption. The distorted wavelength curvature is for the wavelength intervals - 890 to 910 nm and 990 to 1010 nm in the IR region of the spectrum.

Also, the Spectral Spread related calculations was taken to be an average across the three regions of the spectrum. Technical limitations of the spectrometer meant that the influence of wavelength on a single pixel column could not be determined. By extrapolating the trend with 30, 40, 50 ON pixel columns, the spectral spread for a single pixel column was determined. The averages across the three regions were rounded off to nearest integer values for ease of calculation. This method is very rudimentary and further investigation is needed to get a more accurate spectral spread across the spectrum. A higher resolution spectrometer could also provide better results and a better trend across the length (1920 pixels in the X-direction) of the DMD. This can be directly fed to the spectral spread matrix of the model further improving the results.

Finally the model can work autonomously if post-processing steps corresponding to different modulation schemes can be developed and integrated into it. The image sequence depends on the modulation scheme and to analyze the results and get the final EQE of the device under test, post-processing step is necessary. A very promising transform in image processing - Hadamard Transforms which involves simpler computations and subsequently faster processing abilities has been detailed in Appendix B. A post-processing step corresponding to this modulation sequence can be the next step forward to make this model more versatile and utilitarian. Besides other orthogonal transforms like the wavelet transforms and Haar basis functions can be used as potential post-processing steps. The basis functions in the Haar transform can be scaled to different simpler intervals such as [0, 1] or [0, 1/2] and [1/2, 1] thereby providing higher precision than Fourier transforms, which have basis functions in a wider interval $[-\infty, +\infty]$ [38].

Bibliography

[1] International Energy Agency, "Key world energy statistics," *International Energy Agency*, 2017. [Online]. Available: https://www.iea.org/publications/freepublications/publication/KeyWorld2017.pdf

[2] Union of Concerned Scientists, "Our Energy Choices: Coal and Other Fossil Fuels," 2017. [Online]. Available: http://www.ucsusa.org/clean-energy/coal-and-other-fossil-fuels#.WfcT7_krLRY

[3] M. Zeman, J. Melskens, M. Semanová, and Z. Voderadská, "Photovoltaic solar energy: Key to a sustainable energy future," *International Issues & Slovak Foreign Policy Affairs*, vol. XVI, pp. 36–52, 01 2007.

[4] P. Mahtaney, *India, China and globalization: the emerging superpowers and the future of economic development*. Springer, 2007.

[5] Feifei Shen, "China Is Adding Solar Power at a Record Pace - Bloomberg," 2017. [Online]. Available: https://www.bloomberg.com/news/articles/2017-07-19/china-adds-about-24gw-of-solar-capacity-in-first-half-official

[6] Julian Spector, "Coal Down, Renewables Up, India on the Rise in 2035 Energy Outlook | Greentech Media," 2017. [Online]. Available: https://www.greentechmedia.com/articles/read/coal-down-renewables-up-india-on-the-rise-in-2035-energy-outlook#gs.dZ=M3RY

[7] D. Henner, *Renewables 2017: Global Status Report*. Paris: REN21, 2017. [Online]. Available: http://www.ren21.net/wp-content/uploads/2017/06/17-8399_GSR_2017_Full_Report_0621_Opt.pdf

[8] F. Ise, "Photovoltaics report," *Fraunhofer Institute for Solar Energy Systems ISE*, vol. June, 2018. [Online]. Available: https://www.ise.fraunhofer.de/content/dam/ise/de/documents/publications/studies/Photovoltaics-Report.pdf

[9] J. Melskens, S. Heirman, R. Koornneef, M. Elshinawy, and M. Schouten, "Fast Optical Measurement System: Ultrafast external quantum efficiency measurements on silicon solar cells," *Solar Energy Materials and Solar Cells*, pp. 0–1, 2017. [Online]. Available: http://linkinghub.elsevier.com/retrieve/pii/S0927024817303884

[10] A. Smets, J. Klaus, O. Isabella, V. S. Rene;, and Z. Miro, *Solar Energy: The physics and engineering of photovoltaic conversion, technologies and systems.*, 1st ed. Delft, Netherlands: UIT Cambridge, 2015. [Online]. Available: https://www.uit.co.uk/solar-energy

[11] B. H. Hamadani and B. Dougherty, "Solar cell characterization," *Semiconductor Materials for Solar Photovoltaic Cells*, pp. 229–245, 2015.

[12] PVEducation.org, "Quantum Efficiency," 2017. [Online]. Available: http://www.pveducation.org/pvcdrom/quantum-efficiency

[13] T. Markvart and L. Castañer, "Chapter ia-1 - principles of solar cell operation," in *Practical Handbook of Photovoltaics (Second Edition)*, second edition ed., A. McEvoy, T. Markvart, and L. Castañer, Eds. Boston: Academic Press, 2012, pp. 7 – 31. [Online]. Available: http://www.sciencedirect.com/science/article/pii/B9780123859341000015

[14] N. R. E. Laboratory, "Cell Measurements," 2017. [Online]. Available: https://www.nrel.gov/pv/cell-measurements.html

[15] H. Field, "UV-VIS-IR Spectral Responsivity Measurement System for Solar Cells," *National Centre for PV Program*, 1998. [Online]. Available: https://www.nrel.gov/docs/fy99osti/25654.pdf

[16] Adnan Adla, "Instrumentation for quantum efficiency measurement of solar cells - Renewable Energy World," 2010. [Online]. Available: http://www.renewableenergyworld.com/articles/2010/07/instrumentation-for-quantum-efficiency-measurement-of-solar-cells.html

[17] Deepak Bhankot, "Performance Parameters of a Monochromator," 2014. [Online]. Available: http://lab-training.com/2014/04/30/know-the-performance-parameters-of-aas-monochromator/

[18] Newport, "DC Arc Lamps," 2017. [Online]. Available: https://www.newport.com/f/dc-arc-lamps

[19] PVEducation.org, "Spectral Irradiance," 2017. [Online]. Available: http://www.pveducation.org/pvcdrom/properties-of-sunlight/spectral-irradiance

[20] Spectral Products, "Light Sources," 2017. [Online]. Available: http://www.spectralproducts.com/light-source.html

[21] Stanford Research Systems, "About Lock-In Amplifiers," Stanford Research Systems, Tech. Rep., 2014. [Online]. Available: http://www.thinksrs.com/downloads/PDFs/ApplicationNotes/AboutLIAs.pdf

[22] T. Missbach, R. S. L. Straub, T. M. Benkhoff, and G. Siefer, "High-Speed Broadband Quantum Efficiency Determination of Solar Cells," *IEEE Journal of Photovoltaics*, vol. 7, no. 5, pp. 1384–1389, Sep. 2017. [Online]. Available: http://ieeexplore.ieee.org/document/8002574/

[23] ARCOptix_Switzerland, "BASICS: FOURIER TRANSFORM SPECTROMETRY," ARCoptix S A, Neuchatel, Switzerland, Tech. Rep., 2012. [Online]. Available: http://www.arcoptix.com/pdf/Fouriertransformspectrometertutorial.pdf

[24] J. B. Bates and R. B. Kelman, "FOURIER TRANSFORM SPECTROSCOPY*," *Camp. and Maths with Apple. Pergmon Fms Id*, vol. 4, pp. 73–84, 1978. [Online]. Available: https://ac.els-cdn.com/0898122178900202/1-s2.0-0898122178900202-main.pdf?_tid=c60da9b0-bf1a-11e7-966e-00000aacb361&acdnat=1509550917_d13cc6a68e920cdc7f25f44d5add49a5

[25] R. Jóźwicki and M. Rataj, "Fourier spectrometry and its applications," *Opto - Electronics Review*, vol. Vol. 6, No. 4, pp. 233–244, 1998. [Online]. Available: http://yadda.icm.edu.pl/baztech/element/bwmeta1.element.baztech-article-BWA1-0001-0270

[26] Newport.com, "Introduction to FTIR Spectroscopy," Newport Corporation, Tech. Rep., 2015. [Online]. Available: https://www.newport.com/n/introduction-to-ftir-spectroscopy

[27] a. Poruba, M. Vaněček, J. Meier, and a. Shah, "Fourier transform infrared photocurrent spectroscopy in microcrystalline silicon," *Journal of Non-Crystalline Solids*, vol. 299-302, pp. 536–540, 2002.

[28] L. Hod'áková, A. Poruba, R. Kravets, and M. Vaněček, "Fast quantum efficiency measurement of solar cells by Fourier transform photocurrent spectroscopy," *Journal of Non-Crystalline Solids*, vol. 352, no. 9-20 SPEC. ISS., pp. 1221–1224, 2006.

[29] A. Poruba, L. Hodakova, A. Purkrt, J. Holovsky, and M. Vanecek, "Fast quantum efficiency measurement and characterization of different thin film solar cells by fourier transform photocurrent spectroscopy," in *2006 IEEE 4th World Conference on Photovoltaic Energy Conference*, vol. 2, May 2006, pp. 1525–1528.

[30] a. Rshikesan, M. K. Juhl, and T. Trupke, "Estimating the effect of LED based systems of EQE measurement in solar cells," *43rd IEEE Photovoltaic Specialists Conference*, vol. 0, no. 4, pp. 1580–1584, 2016.

[31] B. H. Hamadani, J. Roller, B. Dougherty, and H. W. Yoon, "Fast and reliable spectral response measurements of PV cells using light emitting diodes," *2013 IEEE 39th Photovoltaic Specialists Conference (PVSC)*, pp. 73–75, 2013. [Online]. Available: http://ieeexplore.ieee.org/document/6744102/

[32] J. A. Rodríguez, M. Fortes, C. Alberte, M. Vetter, and J. Andreu, "Development of a very fast spectral response measurement system for analysis of hydrogenated amorphous silicon solar cells and modules," *Materials Science & Engineering B*, vol. 178, pp. 94–98, 2013. [Online]. Available: https://ac.els-cdn.com/S0921510712004904/1-s2.0-S0921510712004904-main.pdf?_tid=b78a6622-bd8e-11e7-8fed-00000aacb35e&acdnat=1509380812_9404f41ef4e2ce3bee1bc1300866a2aa

[33] D. Dudley, W. M. Duncan, and J. Slaughter, "Emerging digital micromirror device (DMD) applications," *Proc.SPIE*, vol. 4985, no. Dmd, p. 14, 2003. [Online]. Available: http://proceedings.spiedigitallibrary.org/proceeding.aspx?doi=10.1117/12.480761

[34] T. Missbach, C. Karcher, and G. Siefer, "Frequency-division-multiplex-based quantum efficiency determination of solar cells," *IEEE Journal of Photovoltaics*, vol. 6, no. 1, pp. 266–271, 2016.

[35] B. Lee, "Texas instruments - introduction to digital micromirror devices (dmds)," *Introduction to Digital Micromirror Devices (DMDs)*, 2008. [Online]. Available: http://www.ti.com/lit/an/dlpa008b/dlpa008b.pdf

[36] Dynasil, "Bandpass Filters | Dynasil," 2017. [Online]. Available: https://www.dynasil.com/product-category/optical-filters/bandpass-filters/

[37] K. M. Takao Tanabe, Masato Shibuya, "Practical method for evaluating optical image defects caused by center artifacts," *Optical Engineering*, vol. 56, pp. 56 – 56 – 9, 2017. [Online]. Available: https://doi.org/10.1117/1.OE.56.8.085103

[38] R. X. Gao and R. Yan, "Wavelets: Theory and applications for manufacturing," *Wavelets: Theory and Applications for Manufacturing*, pp. 1–224, 2011.

[39] N. Lebedev and R. Silverman, *Special Functions & Their Applications*, ser. Dover Books on Mathematics. Dover Publications, 2012. [Online]. Available: https://books.google.nl/books?id=YSzDAgAAQBAJ

[40] S. Chevillard, "The functions erf and erfc computed with arbitrary precision and explicit error bounds," *Information and Computation*, vol. 216, pp. 72–95, Jul. 2012. [Online]. Available: https://www.sciencedirect.com/science/article/pii/S0890540112000697

[41] Chris Woodford, "How do interferometers work? - Explain that Stuff," 2017. [Online]. Available: http://www.explainthatstuff.com/howinterferometerswork.html

[42] D. R. Paschotta, "Interferometers and Types," 2013. [Online]. Available: https://www.rp-photonics.com/interferometers.html

[43] D. K. Graff, "Fourier and Hadamard: Transforms in Spectroscopy," *Journal of Chemical Education*, vol. 72, no. 4, p. 304, 1995. [Online]. Available: http://dx.doi.org/10.1021/ed072p304

[44] W. Pratt, J. Kane, and H. Andrews, "Hadamard transform image coding," *Proceedings of the IEEE*, vol. 57, no. 1, pp. 58–68, 1969. [Online]. Available: http://ieeexplore.ieee.org/document/1448799/

[45] A. Ashrafi, "Walsh-Hadamard Transforms: A Review," *Advances in Imaging and Electron Physics*, vol. 201, pp. 1–55, 2017.

[46] B. K. Harms, R. a. Dyer, S. a. Dyer, T. W. Johnson, J. B. Park, and D. Hall, "An Introduction to Hadmard spectrometry and the multiplex advantage," *IEEE*, pp. 434–438, 1989.

[47] S. S. Agaian, K. Panetta, and A. M. Grigoryan, "Transform-based image enhancement algorithms with performance measure," *IEEE Transactions on Image Processing*, vol. 10, no. 3, pp. 367–382, 2001.

[48] A. Geramita and J. Seberry, *Orthogonal Designs: Quadratic Forms and Hadamard Matrices*, ser. Lecture Notes in Pure and Applied Mathematics. M. Dekker, 1979. [Online]. Available: https://onlinelibrary.wiley.com/doi/abs/10.2307/3314680

A

Interferometry and Types of interferometers

This appendix presents an introduction to the concept of interferometry and details the different types of interferometers (besides Michelson Interferometer) that widely used in the field of Science and Engineering along with their schematic working and their principle applications [41], [42].

A.1. Interferometry

Interferometry is an investigative technique used in the fields of astronomy, optical metrology, spectroscopy, quantum mechanics etc., in which waves (usually electromagnetic waves) are superimposed resulting in the phenomenon of interference. Interferometers are widely used in Science and Engineering for detecting and measuring small displacements, changes in refractive index in the medium of wave propagation, surface irregularities etc., In an interferometer light from the source is split using a beam splitter into 2 waves. A beam splitter is a half-transparent mirror which allows half the light incident to pass through it and the other half is reflected back. The 2 split beams travel different optical paths, are then combined again by superposing resulting in an interference pattern [41]. As the wavelength of the visible light is in the nanometre range, small changes in the differences in the optical paths between the two beams can be detected - as these differences will produce noticeable changes in the interference pattern. Based on the methods of interference, it can be classified into

- **Constructive Interference** – When the 2 waves with the same frequency combine such that the crest of one wave meets the crest of another wave at the same point (in phase with each other) they interfere constructively resulting in a wave with amplitude as the sum of the individual amplitudes.
- **Destructive Interference** - When the 2 waves with the same frequency combine such that the crest of one wave meets the trough of another wave at the same point (out of phase with each other) they interfere destructively resulting in a wave with null amplitude.
- **Partial Interference** - When the waves interfere with each other in all other combinations except constructive and destructive interference, then the resulting amplitude of the wave will be the difference of the individual amplitudes.

A.2. Types of interferometers

- **Fabry-Perot Interferometer** - It was invented in 1897 by Charles Fabry and Alfred Perot, it is also known as an Etalon interferometer and has evolved from the Michelson interferometer.

It is in applications where clearer and sharper fringes that are easier to see and measure are needed. It is mainly used for monitoring slight changes in optical wavelength or frequency.

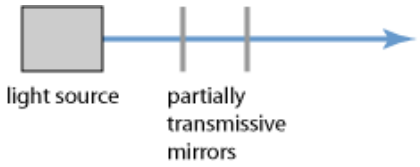

Figure A.1: Simple Schematic of Fabry-Perot Interferometer [42].

- **Mach-Zehnder interferometer** - It was invented by German Ludwig Mach and Swissman Ludwig Zehnder and uses two beam splitters instead of one to produces two output beams, which can be analysed separately. It's widely used in fluid dynamics and aerodynamics for which it was originally developed.

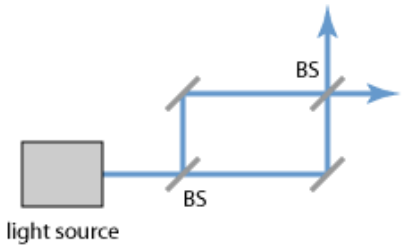

Figure A.2: Simple Schematic of Mach-Zehnder interferometer [42].

- **Fizeau interferometer** - It is named after the French physicist Hippolyte Fizeau and is widely used for making optical and engineering measurements. It is used for the evaluation of the quality of optical components, measurements of flat and spherical optical surfaces and validation of system performance.

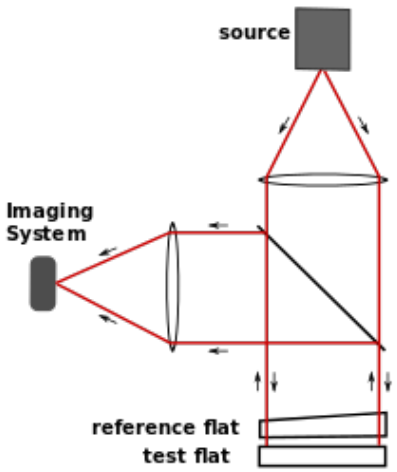

Figure A.3: Simple Schematic of Fizeau interferometer [42].

- **Sagnac interferometer** - It is named after the French physicist Georges Sagnac. This interferometer splits light into two beams that travel in opposite directions around a closed loop or ring. It is also called a ring interferometer. It's widely used in navigational equipments,

such as ring-laser gyroscopes (optical versions of gyroscopes that use laser beams instead of spinning wheels).

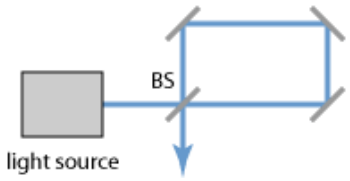

Figure A.4: Simple Schematic of Sagnac interferometer [42].

B

Alternative Modulation Scheme

This appendix gives a brief introduction into Mathematical Transformations and details a promising alternative modulation scheme to the one based on Michelson interferometer which is adopted currently by the DST team in the FOMS prototype.

Mathematical transformations in simple terms relates to the mathematical operations which allow the direct mapping of information from one domain to another and they have a wide range of applications in physical sciences, with spectroscopic studies, imaging techniques and signal compression for data storage being the most prevalent ones [43]. This is due to the fact that it is easier to analyze the mathematical data and results in one domain compared to another. The most widely used transform in spectroscopy studies is the Fourier Transforms and with the development of computers and algorithms that can expedite the calculations, the Fourier mathematics has revolutionized the spectroscopy in the last few decades. The Fourier transforms was thus a natural operator in the image processing domain due to its widespread applications in other fields of study and the presence of a very efficient computational algorithm. But a question arises, if there are other transforms more suitable to image processing than the Fourier transforms and strangely they do.

The main requirements for the image processing applications is that, the transforms should have a two-dimensional operator which has an inverse, it should possess the averaging property and redistribute the energy properly [44]. The symmetric Hadamard matrix transforms fulfills all of these requirements and is better in many aspects than the Fourier transform for image processing.

The Hadamard matrix is a square array of plus (+) ones and minus (-) ones as elements, whose rows (and columns) are orthogonal to one another. In other words if H is a N×N Hadamard matrix, then the product of H and its transpose is the identity matrix [44].

$$HH^T = NI \tag{B.1}$$

where I is the identity matrix. If H is a symmetric matrix, then B.1 reduces to

$$HH = NI \tag{B.2}$$

The smallest order Hadamard matrix is a 2×2 matrix given as:

$$H = \begin{pmatrix} 1 & 1 \\ 1 & -1 \end{pmatrix} \tag{B.3}$$

The Hadamard matrix of order N = 2^p, where p is an integer can be found using the following equation:

$$H_N = H_2 \otimes H_{N/2} \tag{B.4}$$

For example a Hadamard matrix G of order 8, can be found using the above equation to be:

$$G = \begin{pmatrix} H & H \\ H & -H \end{pmatrix} \tag{B.5}$$

The frequency interpretation of the Hadamard matrix is given the sequency change which is shown in figure B.1. Along each row of the Hadamard matrix the frequency is the number of changes in sign - "Sequency", coined by Harmuth [44]. Thus, in this context the Hadamard matrices merely performs the decomposition of a function by a set of rectangular waveforms rather than the sine-cosine waveforms associated with the Fourier transforms.

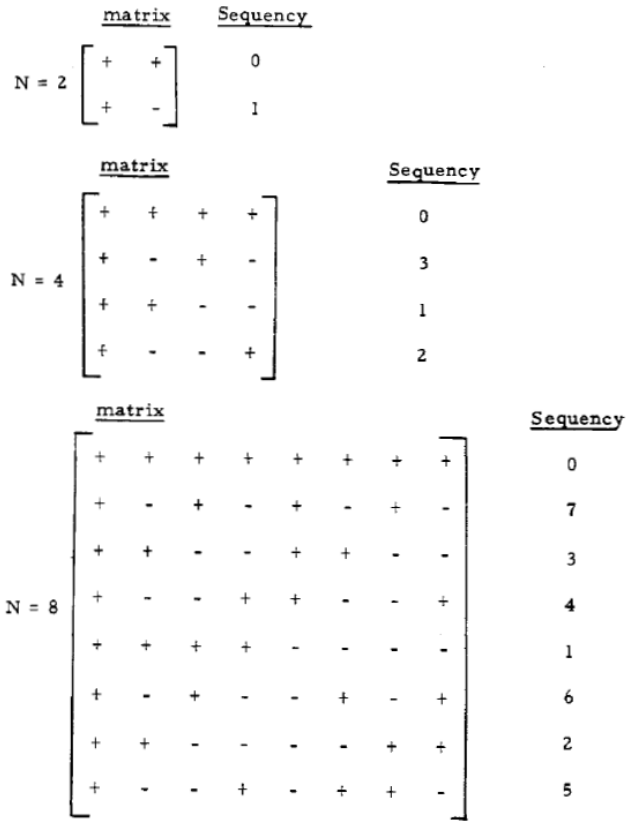

Figure B.1: Hadamard matrices with their sequency for order N - 2,4 and 8 respectively [44].

Since the elements of the Hadamard matrix are either +1 or -1, the calculations involving these matrices requires only additions and subtractions, making their computations less intense and significantly faster than discrete Fourier transforms [45]. In spectroscopy studies where the dominant noise in the measurements is the due to the noise generated in the detector itself, the "signal-to-noise ratio" of the spectrum estimates can be improved by a multiplexing technique offered by the Hadamard transforms[46]. Further it is often easier and efficient from calculation and computation standpoint to deal with real numbers as in Hadamard transforms to complex number as in Fourier transforms [47]. Agaian et al [47], also mentioned that for a negligible trade off in accuracy, the Hadamard transform achieved significantly higher performance enhancements and dramatic improvements in the speed when compared to Fourier transforms. Pratt et al [44] also established that for a 256 by 256 point scene, the Hadamard transforms are about 7 times faster the Fourier transforms. The tolerance to errors in channels (obtained by higher averaging) and possibility of bandwidth reduction are also realized better using Hadamard image coding techniques.

These interesting properties make Hadamard transforms better suited for the spectral analysis

in the Fast Optical Measurement System as well. Bitmap images based on Hadamard series can be generated using Paley Construction principles [48], where the number of white pixels in each image should be a multiple of 2^p and a subsequent post-processing step needs to be developed to analyze and get the desired result from the Hadamard Transforms.